



**TÉCNICO**  
LISBOA

# **Strength and crashworthiness of aircraft composite FRP panels under blast and explosion**

**João Cunha Néné**

Thesis to obtain the Master of Science Degree in

## **Aerospace Engineering**

Supervisors: Prof. Nuno Miguel Rosa Pereira Silvestre  
Dr. António Pedro Carones Duarte

### **Examination Committee**

Chairperson: Prof. Filipe Szolnoky Ramos Pinto Cunha  
Supervisor: Prof. Nuno Miguel Rosa Pereira Silvestre  
Member of the Committee: Prof. Pedro Miguel de Almeida Areias

**April 2021**



To my family





## **Acknowledgments**

I would like to present my sincere gratitude for the guidance provided by my supervisor Professor Nuno Silvestre; I will always admire the knowledge and rigour he transmitted throughout my academic experience. I would also like to thank Doctor António Duarte for his tireless support and motivation provided in the last months; his knowledge and advice allowed me to grow as a student, a future engineer and a person.

To the family I made in Lisbon, my never-ending love and appreciation for enriching the last years of my life.

Last but not least, words are not enough to express how grateful I am for my mother, who gave me the freedom and support to follow my dreams.



## Resumo

Os compósitos laminados de polímeros reforçados com fibras de carbono (PRFC) têm sido crescentemente utilizados em estruturas aeroespaciais (e.g., painéis de fuselagem) sujeitas a risco de ações explosivas. A maioria dos estudos sobre os efeitos explosivos em painéis tem-se focado em configurações planas metálicas, com poucos a investigarem laminados curvos utilizados na fuselagem de aeronaves atuais. O presente estudo tem como objectivo responder a esta limitação, investigando numericamente a influência da curvatura e da geometria de reforços na mitigação dos efeitos do carregamento de uma onda de choque em painéis cilíndricos de PRFC.

Inicialmente, desenvolveu-se e validou-se um modelo numérico de um painel plano de PRFC. Em seguida, realizou-se um estudo numérico sobre a resposta dinâmica e resistência de painéis curvos (sem e com reforços) sujeitos a explosão, capturando os padrões de deformação e modos de rotura, bem como a influência da taxa de deformação nas propriedades dos materiais.

Os resultados mostraram que a resistência à explosão dos painéis é sensível à geometria da superfície incidente: a configuração convexa apresentou maior resistência ao carregamento explosivo do que a côncava. Sob condições em que os painéis não falhavam, o aumento da curvatura resultou num menor carregamento induzido pela onda de choque devido ao aumento do ângulo de incidência. Adicionalmente, as deformações diminuíram devido ao aumento da rigidez dos painéis. Finalmente, verificou-se que a inclusão de reforços resulta em reduções das deformações dos painéis e do dano nos laminados, com os reforços com secção em  $\Omega$  a conduzirem aos melhores desempenhos.

**Palavras-chave:** Carregamento explosivo, PRFC, painéis reforçados curvos, modelo numérico, resposta dinâmica, modos de rotura.



## Abstract

Carbon fibre-reinforced polymer (CFRP) composite laminates are increasingly being used in aerospace structures (e.g., fuselage panels) at risk of blast actions. Most studies regarding the effects of blast loading in panels have focused on flat configurations with metal-based materials, with few addressing the response of curved laminates used in the fuselage of current aircraft models. This study aims to address this limitation by numerically investigating the influence of the curvature and stiffeners' geometry on the mitigation of the effects of a shock wave loading in single-curved CFRP panels.

Initially, a numerical model of a flat CFRP panel was developed and validated. Then, the dynamic response and blast resistance of curved panels (without and with reinforcements) was studied, capturing the deformation patterns and failure modes, as well as the influence of strain rate on the material properties.

The results showed that the blast resistance of the panels is sensitive to the geometry of the incident surface: the convex configuration shows higher resistance to blast loading than its concave counterpart. For blast conditions below a loading threshold, the increase of the curvature resulted in a higher dissipation of the loading from the shock wave due to the higher angle of incidence. Additionally, the deformations also decreased due to an increase of the geometric stiffness of the panels. Finally, the addition of structural reinforcements was proven to reduce both the maximum deformation of the panels and damage of the laminates, with the  $\Omega$ -shaped stringers outperforming the remaining ones studied.

**Keywords:** Blast loading, CFRP, curved stiffened panels, numerical model, dynamic response, failure mechanisms.



# Contents

Acknowledgments . . . . .	v
Resumo . . . . .	vii
Abstract . . . . .	ix
List of Tables . . . . .	xiii
List of Figures . . . . .	xv
Nomenclature . . . . .	xvii
Acronyms . . . . .	xxi
<b>1 Introduction</b>	<b>1</b>
1.1 Scope and motivation . . . . .	1
1.2 Objectives . . . . .	3
1.3 Document outline . . . . .	4
<b>2 Background</b>	<b>5</b>
2.1 Explosive blast loading . . . . .	5
2.1.1 Explosion and shock wave . . . . .	5
2.1.2 Influence of explosive charge . . . . .	6
2.1.3 Blast loading types . . . . .	8
2.1.4 Reflected pressure and impulse . . . . .	8
2.1.5 Blast models . . . . .	9
2.2 FRP composite laminates . . . . .	11
2.2.1 Basic concepts . . . . .	11
2.2.2 Laminate theory . . . . .	12
2.2.3 Damage models . . . . .	13
2.2.4 Applications in the aerospace industry . . . . .	16
2.3 Blast response of FRP panels . . . . .	17
<b>3 Numerical model</b>	<b>25</b>
3.1 Description of the model . . . . .	25
3.1.1 Geometry . . . . .	25
3.1.2 Mesh . . . . .	27
3.1.3 Materials . . . . .	29

3.1.4	Strain rate . . . . .	31
3.1.5	Blast load modelling and boundary conditions . . . . .	32
3.2	Validation of the numerical model . . . . .	33
<b>4</b>	<b>Results and discussion</b>	<b>39</b>
4.1	Dynamic response analysis . . . . .	39
4.2	Influence of panel curvature on the blast response . . . . .	50
4.3	Influence of structural reinforcements . . . . .	56
<b>5</b>	<b>Conclusions</b>	<b>63</b>
5.1	Concluding remarks . . . . .	64
5.2	Future developments . . . . .	65
	<b>References</b>	<b>67</b>



# List of Tables

- 2.1 Heat of detonation of commonly used explosives . . . . . 7
- 2.2 Equivalent mass factors . . . . . 7
  
- 3.1 Geometric data of the reference panel . . . . . 26
- 3.2 Geometric data and mesh of the I-, C-, J- and  $\Omega$ -shaped stringers . . . . . 27
- 3.3 Material parameters for the CFRP IM7/8552 lamina . . . . . 29
- 3.4 Cohesive properties for the adhesive Redux 312 . . . . . 31
- 3.5 Experimental test conditions . . . . . 34



# List of Figures

1.1	Result of the in-board explosion on Daallo Airlines flight 159 . . . . .	1
1.2	CFRP composite usage (in green) in the Airbus A350 . . . . .	2
2.1	Ideal blast wave's pressure-time history . . . . .	6
2.2	Surface representation of $c_{r\alpha}(\alpha, P_{so})$ . . . . .	9
2.3	Schematic representation of the blast wave reflection formulation . . . . .	10
2.4	Common types of fibre-reinforced materials: (a) discontinuous; (b) unidirectional; (c) bi-directional; (d) woven . . . . .	12
2.5	Equivalent stress-equivalent displacement relation . . . . .	15
2.6	Fracture growth modes: (a) Mode I (opening/peeling); (b) Mode II (sliding); (c) Mode III (tearing) . . . . .	16
2.7	(a) Maximum deflection-time history and (b) effect of blast impulse on the maximum deflection of a CFRP laminate . . . . .	18
2.8	Damage progression on the (a) carbon and (b) glass FRP panels for increasing pressure loading values . . . . .	19
2.9	Deformation modes of CFRP laminate panels with different radii of curvature . . . . .	20
2.10	Centre point deflection history of CFRP laminate panels with different radii of curvature . . . . .	20
2.11	Delamination damage area with increasing blast impulses for carbon and glass fibre laminates . . . . .	21
2.12	Schematic representation of the blast-induced delamination in FRP panels with (a) bounded and (b) clamped boundary conditions . . . . .	22
2.13	Influence of ply orientation on the energy dissipated by the failure modes . . . . .	23
3.1	Geometry and mesh of the reference panel . . . . .	26
3.2	Mesh convergence study . . . . .	28
3.3	Composite layups . . . . .	30
3.4	Boundary conditions . . . . .	33
3.5	Schematic representation of the boundary conditions in the FEM . . . . .	34
3.6	Far-field measured (dashed lines) and numerical (solid lines) overpressure-time profiles . . . . .	35
3.7	Effect of blast impulse on the maximum out-of-plane displacement . . . . .	36
3.8	Ply rupture regions: (a) experimental, (b) numerical and (c) numerically replicated . . . . .	36

4.1	Overpressure time-history of free-air blast with $W_e = 100$ g and SOD = 1 m measured in the centre-point of the panel . . . . .	40
4.2	Distribution of the incident overpressure (in Pa) due to the shock wave in the (a) convex and (b) concave surfaces of the panel for the same post-detonation time ( $t=1.13$ ms) . . . . .	40
4.3	Time-history of the out-of-plane displacement prior to damage initiation along the z-axis for the (a) convex (CV) and (b) concave (CC) configuration and along the x-axis for the (c) convex and (d) concave configuration. . . . .	42
4.4	Surface distribution of damage in each ply for the concave configuration by the end of the blast loading ( $t = 2.0$ ms). . . . .	43
4.5	Surface distribution of damage in each ply for the convex configuration by the end of the blast loading ( $t = 2.0$ ms). . . . .	44
4.6	Total energy time history of the model for the (a) convex and (b) concave configuration. . . . .	46
4.7	Time history of the components of the internal energy for the (a) convex and (b) concave configuration. . . . .	48
4.8	Time history of the ratio of artificial strain energy to internal energy for the convex (CV) and concave (CC) configuration. . . . .	49
4.9	Maximum value of the work of external forces per radius of curvature, $r$ , for charge masses of 60g and 100g of TNT. . . . .	50
4.10	Influence of the curvature on the centre of mass height ( $y_{CM}$ ) and the second moment of area ( $I_{xx}$ ) . . . . .	51
4.11	Deformed shapes of panel (a) R500 and (b) R1000 prior to damage initiation ( $t = 1.13$ ms) . . . . .	52
4.12	Time history of the (a) kinetic energy and (b) elastic strain energy for $W_e = 100$ g . . . . .	53
4.13	Influence of curvature on the percentage of damaged elements at the end of the blast loading for $W_e = 100$ g . . . . .	54
4.14	Influence of curvature on the surface distribution of damage for $W_e=100$ g by the end of the blast loading ( $t = 2.0$ ms) . . . . .	55
4.15	Deformed shapes of the five panels at $t = 1.10$ ms (scale factors = 20, 20, 1, for X, Y, Z axes, respectively) . . . . .	56
4.16	Time history of the (a) kinetic energy and (b) elastic strain energy for each model . . . . .	57
4.17	Energy dissipated by damage in the skin, stringers and adhesive interface for each configuration . . . . .	59
4.18	Debonding on (a) the surface and (b) the cross-section of the panel $\Omega$ at $t = 2.0$ ms . . . . .	60

# Nomenclature

## Greek symbols

$\alpha$  Angle of incidence

$\delta_{eq}, \delta_{eq}^0, \delta_{eq}^t$  Equivalent displacements

$\varepsilon$  Strain tensor

$\dot{\varepsilon}$  Strain rate

$\nu$  Poisson's ratio

$\rho$  Mass density

$\sigma$  Stress tensor

$\theta$  Relative rotation of the fibres

$\theta_x, \theta_y, \theta_z$  Rotations

## Roman symbols

$\mathbf{C}_d$  Damaged elasticity matrix

$c_{r\alpha}$  Reflection coefficient

$d_f, d_m, d_s$  Damage variables

$d_x, d_y, d_z$  Displacements

$E_{nn}, E_{ss}, E_{tt}$  Material stiffness in cohesive layer

$F_f^t, F_f^c, F_m^t, F_m^c$  Failure indices

$G_n^{cr}, G_s^{cr}, G_t^{cr}$  Fracture energies in cohesive layer

$G_{ft}^{cr}, G_{fc}^{cr}, G_{mt}^{cr}, G_{mc}^{cr}$  Fracture energies

$i_r^+, i_r^-$  Reflected impulse

$i_s^+, i_s^-$  Incident impulse

$K_{nn}, K_{ss}, K_{tt}$	Stiffness coefficient
$P_0$	Ambient pressure
$P_s$	Incident overpressure
$P_{r\alpha}$	Peak reflected overpressure
$P_{ro}$	Peak normal reflected overpressure
$P_{so}$	Peak overpressure
$t_A$	Time of arrival of the shock wave
$t_d$	Duration time of the positive pressure phase
$t_n^0, t_s^0, t_t^0$	Maximum traction stress
<b>M</b>	Damage operator matrix
<b>b</b>	Decay coefficient
<b>E</b>	Young's modulus
<b>G</b>	Shear modulus
$H^d$	Heat of detonation
<b>K</b>	Equivalent mass factor
$L_c$	Characteristic length
<b>N</b>	Number of plies/sequence of plies
<b>R</b>	Stand-off distance
<b>r</b>	Radius of curvature
<b>W</b>	Mass of explosive
$W_e$	Equivalent mass of TNT
$X_T, X_C$	Strength in fibre direction
$Y_T, Y_C$	Strength in transverse direction
<b>Z</b>	Scaled distance

### Subscripts

1, 2, 3	Material directions
$x, y, z$	Cartesian components

C, c Compressive  
f Fibre  
m Matrix  
n, s, t Normal and the two shear directions in cohesive layer  
nn, ss, tt Normal and the two shear directions in cohesive layer  
s Shear  
T, t Tensile

### **Superscripts**

+ Positive pressure phase  
- Negative pressure phase  
0 Initial  
c Compressive  
cr Critical  
f Final  
t Tensile





# Acronyms

**BK** Benzeggagh-Kenane.

**CFRP** Carbon fibre-reinforced polymer.

**COCOMAT** Improved Material Exploitation at Safe Design of Composite Airframe Structures by Accurate Simulation of Collapse.

**DAHS** Design and Analysis of Hardened Structures to Conventional Weapons Effects.

**DOF** Degrees of freedom.

**FE** Finite element.

**FEA** Finite element analysis.

**FEM** Finite element model.

**FRP** Fibre-reinforced polymer.

**MAXS** Maximum nominal stress criterion.

**POSICOSS** Improved Postbuckling Simulation for Design of Fibre Composite Stiffened Fuselage Structures.

**S4** 4-node shell element.

**S4R** 4-node shell element with reduced integration.

**SOD** Stand-off distance.

**TNT** Trinitrotoluene.

**UD** Unidirectional.



# Chapter 1

## Introduction

### 1.1 Scope and motivation

Civil aviation has been a target for acts of aggression and terrorism since the beginning of the 20<sup>th</sup> century. Cases of bombing attacks go back to 1933, when an on-board explosive device made of nitroglycerin detonated on the cargo hold of a Boeing 247D operated by United Airlines [1]. A series of attacks throughout the years has shown the vulnerability of civilian aircraft to the blasts caused by in-cabin bombs, liquid explosives and later by plastic charges hidden inside laptops and other electronic devices, at the great expense of human lives. Figure 1.1 shows the results of an internal explosion aboard Daallo Airlines flight 159 on February 2016 about 15 minutes after take-off, when the plane was at a height of around 11000ft (3350m). Besides being useful to ensure the structural integrity and safety of people in a wide range of civil and military vehicles and infrastructures at risk of explosive blasts, the study and understanding of blast loading in structures led to the development of blast-resistant materials and structures. Traditional blast-resistant structures capable of withstanding the loading from an explosive shock wave have been designed in a bulky and solid way, resulting in costly solutions with poor operational performance.



Figure 1.1: Result of the in-board explosion on Daallo Airlines flight 159 [2].

Aerospace structures, and more specifically aircraft fuselages, are subjected to a complex combination of loads and their design must follow conflicting requirements of strength, stiffness and weight. In this context, composite materials have become popular over the years, increasingly being used in a wide range of structural applications due to their advantages such as high specific strength and stiffness, resistance to corrosion, the ability to adjust and optimize their properties as per loading requirements and potential weight savings, among others [3, 4]. Lower aircraft weight results in an improvement of the fuel efficiency, greater flight range, increase in profit margins for the airlines and reduction of the global environmental impact [5].

Recently, carbon fibre-reinforced polymer (CFRP) composites have been widely used in the design of primary structures of a new generation of commercial aircraft. CFRP account for 53% of the structural weight of one of Airbus' latest commercial aircraft models to date, the Airbus A350, being used in the entire fuselage (including stringers, skin panels, frames, doublers, passenger and cargo doors), wing skins, wing box and empennage, as shown in Figure 1.2 [5].

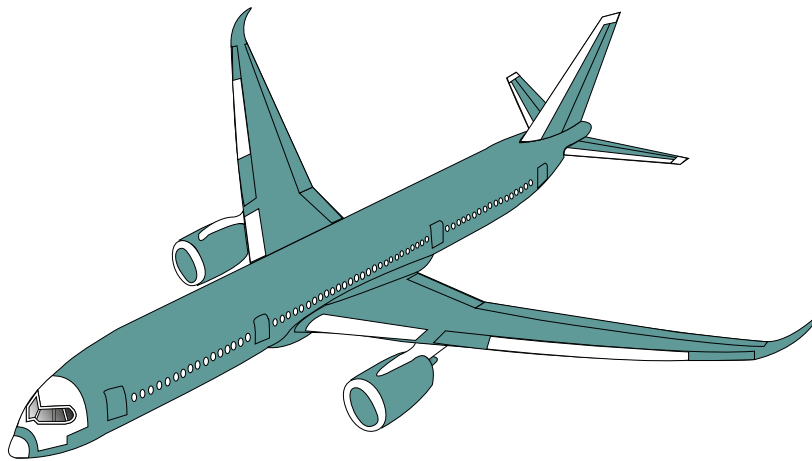


Figure 1.2: CFRP composite usage (in green) in the Airbus A350.

The main drawback that the use of composite materials present is their brittle response specially under high strain rate loading events, as in the case of a shock wave generated by an explosion, exhibiting poor matrix dominated properties in the transverse direction and weak through thickness properties. Moreover, while conventional metals (i.e., steel and aluminium alloys) have the ability to absorb a large amount of energy as they plastically deform, fibre-reinforced polymer (FRP) laminates experience a series of complex brittle-like damage processes under explosive blast loading such as matrix cracking, fibre rupture and delamination at much lower strains.

Research into the explosive limits of commercial aircraft have been made over the last 30 years in order to understand the complex loads and damage resistance on such structures, specially in the case of in-cabin explosions. Experimental tests have been performed by detonating explosive charges inside the cabin of commercial aircraft [6] or by studying the blast response of fuselage panels [7]. The

latter case, however, presents some limitations, as the panels are unable to account for the dynamic large-scale effects inside of an aircraft fuselage [2]. Another challenge is to take into consideration the effect of pressurization and gravity loads at cruising altitudes, as these effects were found to significantly increase the damage under certain blast loading conditions [7]. These blast tests have high costs and generally only provide the final damage pattern, not giving information on the dynamic deformation process during the explosive event. As such, finite element models present a reliable complementary approach to overcome the limitations of experimental setups.

A large body of work into the blast response of panels has been published, focusing mainly on the response of metal-based composite materials [8–11]. While there are finite element models capable of assessing the deformation blast loading in these surfaces, the lack of literature regarding the field of composite materials, especially concerning the strain rate sensitivity of FRP composites at high strain rates induced by blast loading, presents a challenge to numerical modelling. In recent years, experimental and numerical investigations into the deformation and failure process of FRP composites in air blasts have been published, almost entirely restricted to flat configurations [12–15], with few studies addressing the dynamic response of fibre-reinforced curved panels [16, 17]. Recently, however, the interest in curved panels for blast mitigation purposes has increased due to the additional stiffness under explosive blast loads by virtue of their spatial curvatures [8]. At the time of writing this work, no research into the blast response of structurally-reinforced CFRP curved panels is available in the literature.

This work comes after the investigation started in the COCOMAT project [18] and followed in the dissertations of Pereira [19], Silva [20] and Martins [21] into CFRP fuselage panels.

## 1.2 Objectives

This work aims to investigate, through numerical simulations carried out in Abaqus/Explicit (version 6.14), the dynamic response of singly-curved CFRP laminate panels, representative of a fuselage section, under explosive blast loading. The objectives of this dissertation are:

- to implement a numerical model capable of simulating the loading of a shock wave due to a free-air explosion and the deformation process and failure initiation and evolution in CFRP laminate structures with or without structural reinforcements (stringers). The numerical models will be validated using experimental data available in the literature;
- to investigate the influence of geometry, namely convex and concave configurations, in the blast response and failure modes;
- to assess the influence of the radius of curvature on the strength and failure modes of the panels;
- to identify the effect of stringer cross-section geometry (T-, I-, C-, J- and  $\Omega$ -shaped) on blast mitigation.

## 1.3 Document outline

This work is divided into four main sections, following the brief introduction presented in the current chapter.

Chapter 2 contains a literature review of the concepts necessary to support the study on blast loading and the response of FRP structures. This includes a description of the blast phenomenon, the fundamentals of FRP composite materials with a focus on aerospace applications and lastly a review of published research on the blast performance of FRP composite materials.

Chapter 3 covers the detailed description of the numerical models developed in this work, followed by a validation based on the experimental and numerical research carried out by Gargano et al. [13, 14], who also studied the dynamic response of CFRP laminate panels loaded by the shock wave caused by a free-air explosive blast.

In chapter 4, the numerical results regarding the deformation patterns, failure modes and failure progression are reported and discussed.

Finally, chapter 5 presents the conclusions of this dissertation and provides recommendations for future work.

# Chapter 2

## Background

In this chapter it is presented an overview of the published research and the underlying theory regarding the response of fibre-reinforced polymer (FRP) panels to dynamic loads under explosive events.

### 2.1 Explosive blast loading

This section provides a comprehensive review of the blast phenomenon, presenting a description of the loading, initiation and propagation of a shock wave in the air, followed by an insight on the modelling of a pressure-time profile of an explosive shock wave.

#### 2.1.1 Explosion and shock wave

The blast caused by the detonation of conventional explosives originates a localized release of energy in which the highly compressed and hot gases expand, resulting in a shock wave (also called blast wave). The shock wave expands rapidly, propagating at a speed faster than the speed of sound, causing an almost instantaneous change in the gas dynamic conditions.

The ideal overpressure-time curve of a blast wave at a stationary point some distance from the detonation point is presented in Figure 2.1.

As the blast wave arrives at the reference point, there is an instant increase from ambient pressure ( $P_0$ ) to the peak overpressure ( $P_{so}$ ), also known as incident pressure, followed by an exponential decrease to  $P_0$ , which forms the positive pressure phase. The time it takes since the time of arrival ( $t_A$ ) to the pressure to reach  $P_0$  again is known as the duration time ( $t_d$ ). From that point, the pressure decreases further until it stabilizes. This last phase, known as negative pressure phase, is longer in duration than the positive phase but lower in amplitude and can usually be neglected. In the case of composite panels which have weak through thickness properties, the stress level in the positive phase is much larger than in the negative phase and therefore, any damage inflicted due to tensile loads will occur at the positive phase, supporting the accept of ignoring the negative pressure phase [22].

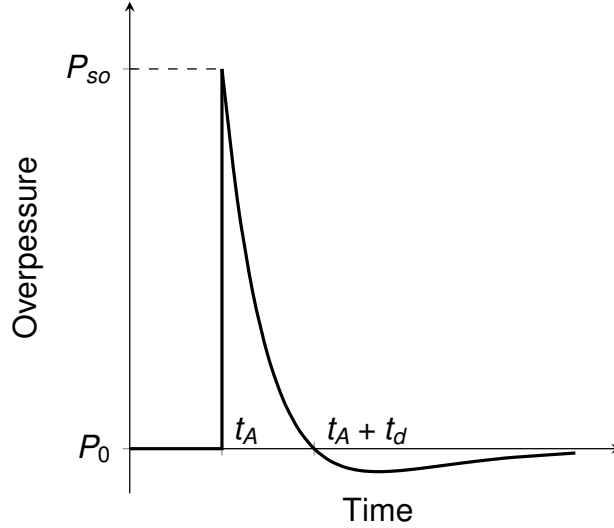


Figure 2.1: Ideal blast wave's pressure-time history.

The exponential decrease in the incident pressure can be modeled by the Friedlander's equation [23],

$$P_s(t) = P_{so} \left( 1 - \frac{t}{t_d} \right) e^{-b \frac{t}{t_d}}, \quad (2.1)$$

where the decay coefficient ( $b$ ) is an intensity characteristic of the blast wave system, calculated using experimental data.

The impulse is an important aspect to evaluate the damage ability of the blast. It depends on the peak overpressure and duration of blast and is defined by the area under the overpressure-time curve. The positive pressure phase impulse ( $i_s^+$ ) can be given by

$$i_s^+(t) = \int_{t_A}^{t_A+t_d} P_s(t) dt = \frac{P_{so} t_d}{b^2} (b - 1 + e^{-b}). \quad (2.2)$$

### 2.1.2 Influence of explosive charge

The main parameters that define a blast loading are the relative distance between the detonation point and the structure of interest, know as stand-off distance (SOD), the mass and type of explosive and the geometry of the target structure.

As the SOD increases, the peak overpressure and velocity of the blast wave rapidly decrease. In fact, two charges of different explosive mass and distance can result in the same overpressure value. By introducing a dimensionless scaled parameter, it is possible to predict blast parameters of the detonation for the same value of the scaled parameter. According to the Hopkinson scaling law, two explosive charges of different masses and similar geometry produce a similar blast wave for the same scaled distances and atmospheric conditions . The scaled distance ( $Z$ ) in this theory is given by [22],

$$Z = \frac{R}{\sqrt[3]{W}}, \quad (2.3)$$

where  $R$  is the SOD and  $W$  is the mass of the explosive.



For conditions under which the target structure is located within the fireball resulted from the detonation of an explosive charge, the expanding gas products dominate the loading and the shock wave can be neglected. Under this condition, the explosion is deemed as near-field. When the target is outside the fireball (typically at a distance within 10 to 20 times the radius of a spherical charge), the effects of the fireball can be disregarded and the explosive event is considered far-field [12].

Despite the variety of existing types of explosives, TNT (Trinitrotoluene) is used as a reference for the calculation of blast parameters. In order to obtain the blast parameters needed to replicate realistic overpressure-time curves for conventional explosives, the equivalent TNT method is most commonly used. In this method, the mass of an explosive can be expressed as an equivalent TNT mass ( $W_e$ ) by using the ratio of the heat produced in detonation, defined as

$$W_e = W \frac{H^d}{H_{TNT}^d}, \quad (2.4)$$

where  $W$  is the mass of the explosive,  $H^d$  is the heat of detonation of the explosive and  $H_{TNT}^d$  is the heat of detonation of TNT. The heat of detonation of commonly used explosives is presented in Table 2.1.

Table 2.1: Heat of detonation of commonly used explosives (adapted from [23]).

Type of explosive	Heat of detonation [MJ/kg]
TNT	4.10-4.55
C4	5.86
RDX	5.13-6.19
PETN	6.69
Nitroglycerin	6.30

The DAHS (Design and Analysis of Hardened Structures to Conventional Weapons Effects) Manual [24] provides an equivalent mass factor ( $K$ ) of commonly used military explosives, which allows to obtain the same values of pressure or impulse for the blast waves originated by different explosive charges. The equivalent TNT mass,  $W_e$ , is thus defined as

$$W_e = KW, \quad (2.5)$$

with the values of  $K$  for a charge of C4 being presented in Table 2.2.

Table 2.2: Equivalent mass factors (adapted from [25]).

Explosive Type	Equivalent mass factor		
	Peak Over-Pressure	Impulse	Pressure Range [MPa]
C4	1.20	1.19	0.07 to 1.38
	1.37		1.38 to 20.70

### 2.1.3 Blast loading types

There are mainly four different types of blasts depending on the relative position of the explosive source and the structure and the distance above ground, which result in different blast loadings onto a structure: free-air blasts, air blasts, surface blasts and internal blasts. In free-air blasts, the explosion occurs in the air, propagating spherically outwards and interacting directly with the structure with no interference from other obstacles. In air blasts, the explosive charge is also detonated in the air, but, contrary to free-air blasts, the blast wave interacts with the ground prior to arriving at the structure. Surface blasts occur almost at ground level and the blast wave immediately interacts with the ground, propagating hemispherically. Finally, internal blasts are defined by the detonation of an explosive inside a structure, where the blast waves propagate and interact with the different walls, reflecting the shock waves and amplifying the effects of the dynamic pressure.

### 2.1.4 Reflected pressure and impulse

As stated previously, the blast wave interacts with the environment as it propagates. When encountering a rigid surface, the shock wave is reflected, creating a pressure build up that causes the reflected pressure to be higher than the incident pressure. When considering an ideal linear-elastic case, the air particles are allowed to bounce back freely from the surface and the reflected pressure is equal to the double of the incident pressure. However, the non-linearity of the blast wave, in which the reflection of the air particles is obstructed by subsequent particles, increases the incident pressure to a peak reflected pressure, which is the pressure experienced by the structural surface [23]. The magnitude of the reflected pressure depends mainly on the blast parameters and angle of incidence ( $\alpha$ ) of the shock wave [22], which is defined by the orientation of the normal of the surface with respect to the travel direction of the shock wave.

The peak reflected overpressure ( $P_{ro}$ ) relates to  $P_0$  and  $P_{so}$  by

$$P_{ro} = 2P_{so} \frac{4P_{so} + 7P_0}{P_{so} + 7P_0}. \quad (2.6)$$

For Equation (2.6), it was assumed that the explosion takes place at standard sea level, the air behaves as an ideal gas and the angle of incidence is zero. As the equation indicates, the ratio  $P_{ro}/P_{so}$  is not constant, varying between 2 and 8. Experimental studies, however, found this ratio to be even higher for blast conditions in which the previous assumptions are not verified [22, 23].

The effect of  $\alpha$  in the resulting reflection and, consequently, the blast loading on the structure is taken into account by introducing the reflection coefficient ( $c_{r\alpha}$ ), defined as

$$c_{r\alpha} = \frac{P_{r\alpha}}{P_{so}}, \quad (2.7)$$

with  $P_{r\alpha}$  being the peak reflected pressure for a given  $\alpha$ . Figure 2.2 shows the influence of  $\alpha$  and  $P_{so}$  on the reflection coefficient,  $c_{r\alpha}$ , based on the parameterized curves given by Karlos and Solomos [23].

In general, the reflected pressure value decreases as  $\alpha$  increases, being maximum in the case of a

normal reflected wave and minimum for an angle of incidence of  $90^\circ$ . In the case of air blasts, in which the shock wave is reflected by the ground prior to arriving at the target (depicted in Figure 2.2), when the angle of incidence exceeds  $40^\circ$ , the reflected pressure wave and incident wave merge, creating, in some cases, a new wave with a pressure higher than the single reflected pressure wave - a phenomenon known as Mach stem. For large values of incident overpressure ( $P_{so} > 3.50\text{MPa}$ ), the angle of incidence may be neglected, as the normal reflected pressure,  $P_{ro}$ , will have a value up to 25% bigger than the peak reflected pressure,  $P_{r\alpha}$ , when Mach Stem occurs. For small and moderate peak overpressures ( $0.01 < P_{so} < 3.50\text{MPa}$ ), however, the angle of incidence should be taken into consideration, as assuming a normal reflected pressure will underestimate the values of  $P_{r\alpha}$  for the range of  $\alpha$  between  $40^\circ$  and  $55^\circ$  [23].

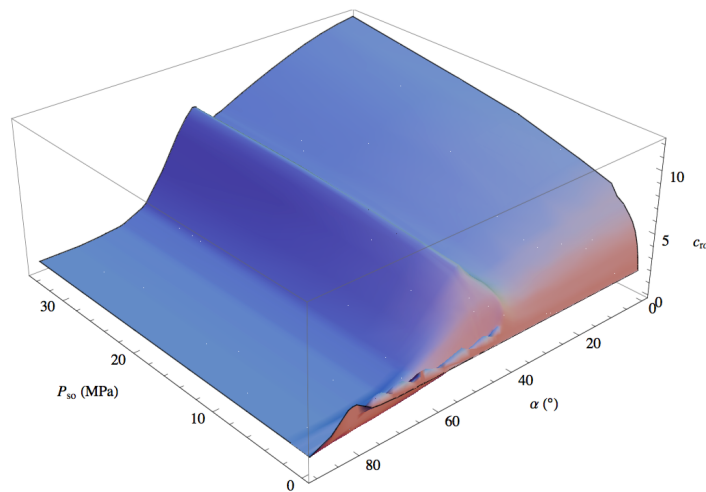


Figure 2.2: Surface representation of  $c_{r\alpha}(\alpha, P_{so})$  [2].

The reflected pressure-time curve follows a variation similar to that of the incident overpressure, shown in Figure 2.1. As such, Equation (2.1) can be used in an analogous way for the case of the reflected pressure, as the variation in time is governed by the same time scales as the incident pressure. The reflected impulse can be determined by using Equation (2.2), replacing  $P_{so}$  by  $P_{r\alpha}$ .

### 2.1.5 Blast models

Two main approaches can be used when modelling the detonation of an explosive charge, which can be either empirical or fully coupled.

Empirical models use idealized pressure-time properties based on correlation with experimental data to model the effects of a blast. Kingery and Bulmash [26] developed charts based on experimental studies to obtain the blast parameters from explosive tests using charges of TNT for both free-air and surface blasts valid for a range of data of  $Z \in [0.05, 40] \text{ m/kg}^{1/3}$ . Using this data, high-order polynomial equations can be fitted to describe the overpressure-time profile of a blast wave. This approach is the most used and accepted for the determination of blast parameters, having been implemented on a series of empirical models [22].

CONWEP (Conventional Weapons Effects Programme) is the most recognised empirical model implemented in finite element commercial codes such as Abaqus/Explicit and LS-DYNA [22], developed to simulate the effects of a blast produced by conventional (i.e., non nuclear) explosives for both spherical and hemispherical blasts. This model is based on the approach proposed by Kingery and Bulmash and has the best overall agreement with experimental data, when compared to other empirical models, such as BlastX and SHOCK [22]. The CONWEP model allows to obtain realistic overpressure amplitudes considering both the positive and negative pressure phases of the shock wave and other blast wave parameters, which are calculated based on a user-defined equivalent mass of TNT at a given distance from the source of the explosion.

The CONWEP model does not require to model the fluid medium in which the shock wave propagates and, therefore, it is not able to account for second-order interactions between reflected pressure waves and the adjacent elements nor the dynamic pressure during a blast event. This presents a limitation when modelling a structure in a semi confined space.

As stated above, neglecting the incident wave reflection may lead to underestimated pressure loadings, whereas assuming the maximum reflection in the entire surface can be overly-conservative, specially for cylindrical geometries. As such, the reflection formulation employed in the CONWEP charge property in Abaqus (represented in Figure 2.3) is used to calculate the peak blast pressure that a structure is subjected to (also referred to as reflected pressure) using the following law [27],

$$P_{r\alpha} = \begin{cases} P_{so}(1 + \cos \alpha - 2 \cos^2 \alpha) + P_{ro} \cos^2 \alpha & \text{if } \cos \alpha \geq 0, \\ P_{so} & \text{if } \cos \alpha < 0. \end{cases} \quad (2.8)$$

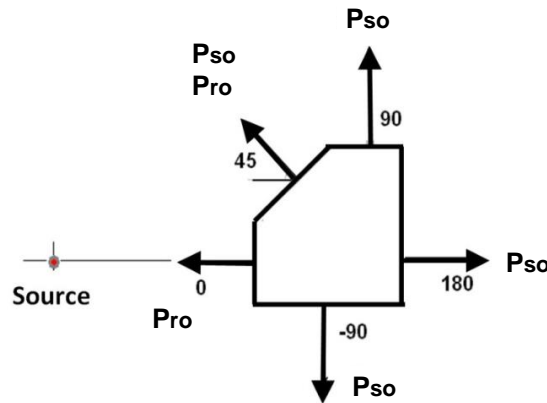


Figure 2.3: Schematic representation of the blast wave reflection formulation (adapted from [27]).

Alternatively, a Coupled Eulerian Lagrangian (CEL) approach permits to model the structural part using a Lagrangian formulation and a fluid domain where the blast waves propagate, using an Eulerian model. This approach presents the advantage of obtaining a complete description of a blast phenomenon, taking into consideration the reflection on solid surfaces and expansion of the hot gases. This allows for a precise and complete simulation of problems with strong coupling between fluid and structure, but demand high computational capacities. Botez and Bredean [28] successfully implemented a CEL approach into Abaqus/Explicit to study the blast effects on a reinforced concrete slab.

## 2.2 FRP composite laminates

Fibre-reinforced polymer (FRP) laminates are extensively used in aerospace structural elements due to their performance benefits regarding weight saving and specific strength and stiffness over conventional metal alloys. The main drawback that composite materials present is having a brittle behaviour, being linearly elastic until failure, which can result in catastrophic failures. In this section, a description of composite materials is provided and constitutive equations are defined based on the Classical Laminate Theory. The reader is then presented with the damage mechanisms and models that are implemented in the finite element analysis (FEA) commercial code Abaqus/Explicit [27] to predict the initiation and evolution of damage in the laminates and structural interfaces of stiffened fibre-reinforced panels. Finally, a brief review on the progress of research of composite materials in the aerospace industry, with special emphasis on their behaviour under blast actions, is presented.

### 2.2.1 Basic concepts

Composite materials are a combination of two or more materials working together to obtain better engineering properties and performance than those of the isolated materials. Most composites are made by a reinforcement material, that can be in the form of fibres or particles, and a base material known as matrix. The matrix serves as a medium for binding the fibres and transferring loads, whereas the fibres provide the composite material with stiffness and strength that are dependent on the direction, while maintaining a low density [3]. This dependency is particularly relevant to match and adjust the material directional properties to the performance requirements in a particular application, as fibres must be oriented for principal stresses, where they present highest strength and moduli.

Fibres can be either continuous or discontinuous and present various directional layouts, as seen in Figure 2.4. In general, discontinuous fibre-reinforced materials exhibit lower strength and modulus, when compared to composites with unidirectional fibres, which show the highest values of strength and modulus in the direction of the fibres and poor transverse properties. Woven fabrics incorporate two sets of yarns interlaced in the lengthwise direction (i.e., warp) and crosswise direction (i.e., weft), providing a more even distribution of the elastic and strength properties of the composite material whilst presenting an efficient and effective alternative from a manufacturing standpoint. However, the undulation of yarns results in the decrease of in-plane stiffness and strength properties of the woven fabric in the warp and weft crossover points, being more prominent for woven fabric patterns with higher frequency of crossovers [29].

A laminate consists of layers called plies or laminae, stacked in a sequence with different orientations (from  $0^\circ$  to  $90^\circ$ ), providing flexibility when looking for a configuration that maximizes the material properties. As stated previously, the presence of anisotropy results in the in-plane strength and stiffness being higher in the direction of the fibres, rather than in the other directions, with this relation prevailing in unidirectional composites rather than in the remaining configurations. Unidirectional fibre-reinforced laminae are defined as orthotropic materials, whose material properties are obtained according to three mutually perpendicular axes [3]. For ply sequences with equal number of plies of  $[0, \pm 45, 90]$  or  $[0, \pm 60]$ , the

composite is said to be quasi-isotropic and the in-plane mechanical properties do not vary with loading direction [4].

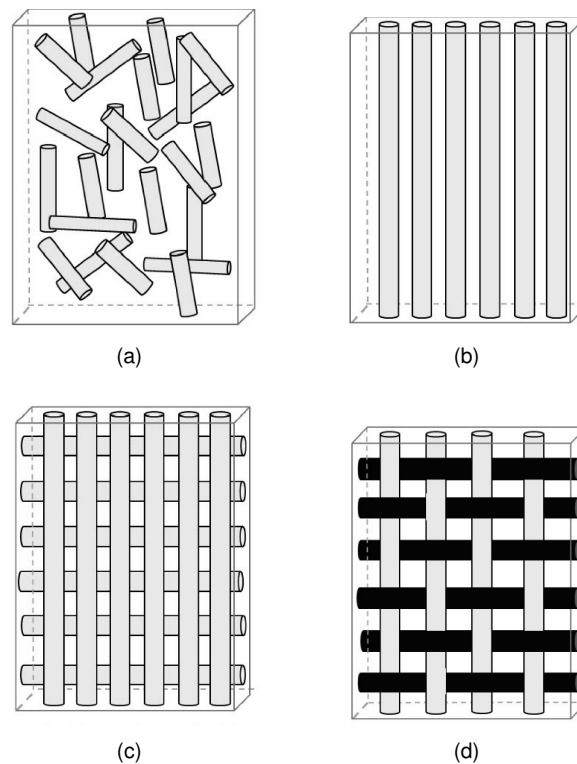


Figure 2.4: Common types of fibre-reinforced materials: (a) discontinuous; (b) unidirectional; (c) bi-directional; (d) woven (adapted from [30]).

## 2.2.2 Laminate theory

Classical Laminate Theory is used in the analysis of fibre-reinforced composites and defines the response of a laminate. To define the mechanical behaviour of a laminate, it is assumed that [4]:

- For two-dimensional plane stress analysis, the strain is constant through the thickness;
- For bending, the strain varies linearly through the thickness;
- The laminate is thin compared with its in-plane dimensions;
- Each layer is quasi-homogeneous and orthotropic;
- Displacements are small compared with the thickness;
- The behaviour remains linear.

Constitutive equations allow to predict strains and stresses by defining the engineering constants associated to an orthogonal local coordinate system with the 1-axis in the fibre direction, the 2-axis perpendicular to the fibres on the plane of the lamina and the 3-axis perpendicular to the plane of the lamina.

For composite laminate panels, the thickness of each single unidirectional ply is small when compared to the panel dimensions and a plane stress condition can be applied. The in-plane stress-strain law for an orthotropic material under plane stress conditions, in relation to the material axes, has the following form,

$$\begin{Bmatrix} \varepsilon_1 \\ \varepsilon_2 \\ \gamma_{12} \end{Bmatrix} = \begin{bmatrix} \frac{1}{E_1} & -\frac{\nu_{12}}{E_1} & 0 \\ -\frac{\nu_{12}}{E_1} & \frac{1}{E_2} & 0 \\ 0 & 0 & \frac{1}{G_{12}} \end{bmatrix} \begin{Bmatrix} \sigma_1 \\ \sigma_2 \\ \tau_{12} \end{Bmatrix}, \quad (2.9)$$

where  $E_1$ ,  $E_2$  are the Young's moduli,  $\nu_{12}$  is the Poisson's ratio and  $G_{12}$  is the (in-plane) shear modulus. Subscript 1 refers to the direction parallel to the fibres and subscript 2 to the transverse direction.

The *laminae* are then defined by four independent variables ( $E_1$ ,  $E_2$ ,  $\nu_{12}$  and  $G_{12}$ ), as  $\frac{\nu_{12}}{E_1} = \frac{\nu_{21}}{E_2}$ .

The value of  $E_1$  is much larger than  $E_2$  and  $G_{12}$ , which shows that a fibre-reinforced composite has higher strength in the direction of the fibres, as stated previously.

### 2.2.3 Damage models

When using fibre-reinforced composites in structural elements there is a need to ensure the levels of safety regarding damage initiation and growth. Currently, a large number of failure criteria for unidirectional composite materials have been developed. Hashin failure criteria, which is based on the work of Hashin and Rotem [31] and Hashin [32], is widely used in structural applications to model four intralaminar damage initiation mechanisms that include fibre rupture in tension ( $F_f^t$ ), fibre kinking in compression ( $F_f^c$ ), matrix cracking in tension ( $F_m^t$ ) and matrix crushing in compression ( $F_m^c$ ), and has been incorporated into many FEA commercial codes such as Abaqus/Explicit [27]. Delamination and failure in adhesives connecting structural elements are often calculated using cohesive zone modelling.

The failure modes included in Hashin's criteria are defined for plane stress conditions as follows,

$$F_f^t = \left( \frac{\hat{\sigma}_{11}}{X_T} \right)^2 + \alpha \left( \frac{\hat{\sigma}_{12}}{S_L} \right)^2 \quad \text{if } \hat{\sigma}_{11} \geq 0 \quad (2.10)$$

$$F_f^c = \left( \frac{\hat{\sigma}_{11}}{X_C} \right)^2 \quad \text{if } \hat{\sigma}_{11} < 0 \quad (2.11)$$

$$F_m^t = \left( \frac{\hat{\sigma}_{22}}{Y_T} \right)^2 + \left( \frac{\hat{\sigma}_{12}}{S_L} \right)^2 \quad \text{if } \hat{\sigma}_{22} \geq 0 \quad (2.12)$$

$$F_m^c = \left( \frac{\hat{\sigma}_{22}}{2S_T} \right)^2 + \left[ \left( \frac{Y_C}{2S_T} \right)^2 - 1 \right] \frac{\hat{\sigma}_{22}}{Y_C} + \left( \frac{\hat{\sigma}_{12}}{S_L} \right)^2 \quad \text{if } \hat{\sigma}_{22} < 0 \quad (2.13)$$

In equations (2.10) to (2.13),  $X_T$ ,  $Y_T$ ,  $X_C$  and  $Y_C$  denote the allowable tensile ( $T$ ) and compressive ( $C$ ) strengths in the material directions ( $X$  - direction of fibres and  $Y$  - direction perpendicular to the fibres),  $S_L$  and  $S_T$  are the allowable longitudinal and transverse shear strengths, respectively, and the coefficient  $\alpha$  determines the contribution of the shear stress to the fibre tension damage criteria.

The initiation criteria presented can be used to obtain the model proposed in Hashin and Rotem [31] by setting  $\alpha = 0.0$  and  $S_T = Y^C/2$  or the model proposed by Hashin [32] by setting  $\alpha = 1.0$ . The onset of damage occurs when any of the failure indices reach unity, i.e., the value of the indexes  $F_f^t$ ,  $F_f^c$ ,  $F_m^t$  and  $F_m^c$  is equal to 1.0.

Abaqus assumes that the response of the laminate is linearly elastic prior to damage initiation. Once damage starts, the values of the stiffness tensor of the lamina are updated to take into account the effect of damage as follows,

$$\boldsymbol{\sigma} = \mathbf{C}_d \boldsymbol{\varepsilon}, \quad (2.14)$$

where  $\boldsymbol{\sigma}$  is the apparent stress,  $\boldsymbol{\varepsilon}$  is the strain and  $\mathbf{C}_d$  is the damaged elasticity matrix, given by

$$\mathbf{C}_d = \frac{1}{D} \begin{bmatrix} (1 - d_f)E_1 & (1 - d_f)(1 - d_m)\nu_{21}E_1 & 0 \\ (1 - d_f)(1 - d_m)\nu_{12}E_2 & (1 - d_m)E_2 & 0 \\ 0 & 0 & (1 - d_s)GD \end{bmatrix}, \quad (2.15)$$

where  $D = 1 - (1 - d_f)(1 - d_m)\nu_{12}\nu_{21}$  and  $d_f$ ,  $d_m$  and  $d_s$  are internal damage variables that characterize fiber, matrix and shear damage, respectively, and are associated to the four modes of damage previously discussed as follows,

$$df = \begin{cases} d_f^t & \text{if } \hat{\sigma}_{11} \geq 0 \\ d_f^c & \text{if } \hat{\sigma}_{11} < 0 \end{cases}, \quad (2.16)$$

$$dm = \begin{cases} d_m^t & \text{if } \hat{\sigma}_{22} \geq 0 \\ d_m^c & \text{if } \hat{\sigma}_{22} < 0 \end{cases}, \quad (2.17)$$

$$d_s = 1 - (1 - d_f^t)(1 - d_f^c)(1 - d_m^t)(1 - d_m^c). \quad (2.18)$$

Abaqus uses the model proposed by Matzenmiller et al. [33] to compute the damage effect. The four damage initiation modes given in Equations (2.10) to (2.13) are applied as damage evolution criteria by substituting effective stresses  $\hat{\boldsymbol{\sigma}}$  for Cauchy stress  $\boldsymbol{\sigma}$  in each mode, following the relation given by

$$\hat{\boldsymbol{\sigma}} = \mathbf{M}\boldsymbol{\sigma}, \quad (2.19)$$

where  $\mathbf{M}$  is the damage operator given as

$$\mathbf{M} = \begin{bmatrix} \frac{1}{(1-d_f)} & 0 & 0 \\ 0 & \frac{1}{(1-d_m)} & 0 \\ 0 & 0 & \frac{1}{(1-d_s)} \end{bmatrix}. \quad (2.20)$$

When damage initiates and evolution has occurred for at least one mode, the damage operator  $\mathbf{M}$ , which is equal to the identity matrix until that point, becomes significant in the criteria for damage initiation of the other modes.



Once any damage criteria is satisfied, material degradation will occur with increasing loading. In order to alleviate the strong mesh and element-type dependency due to the strain-softening behaviour of the material, a characteristic length  $L_c$  is used to transform the constitutive stress-strain model in a stress-displacement model by computing  $\delta = \varepsilon L_c$ , as seen in Figure 2.5.

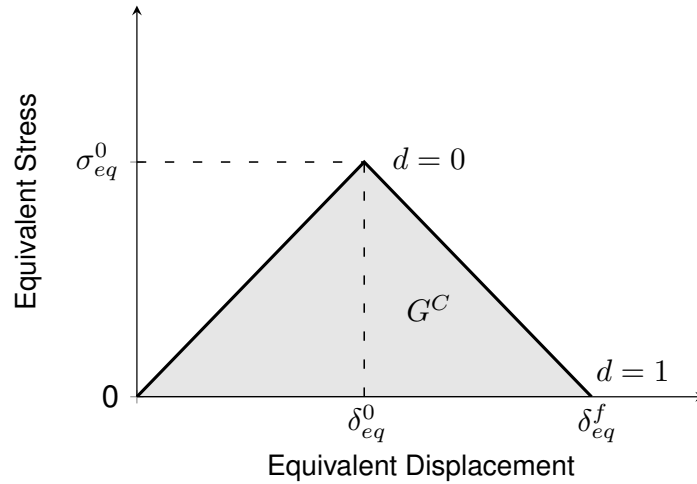


Figure 2.5: Equivalent stress-equivalent displacement relation (adapted from [27]).

The evolution of the damage variables is governed by an equivalent displacement  $\delta_{eq}$ , expressed in terms of the effective stress components, such that each damage mode is represented as a one-dimensional stress-displacement problem [27]. The damage variable for a particular mode can then be expressed by the following relation,

$$d = \frac{\delta_{eq}^f (\delta_{eq} - \delta_{eq}^0)}{\delta_{eq} (\delta_{eq}^f - \delta_{eq}^0)}, \quad (2.21)$$

where  $\delta_{eq}^0$  is the initial equivalent displacement at which the initiation criterion for that mode was met and  $\delta_{eq}^f$  is the displacement at which the material is completely damaged in the failure mode. The values of  $\delta_{eq}^0$  will depend on the elastic stiffness and the strength parameters of the damage initiation criteria, whereas  $\delta_{eq}^f$  can be defined by specifying  $G_{ft}^{cr}$ ,  $G_{fc}^{cr}$ ,  $G_{mt}^{cr}$ , and  $G_{mc}^{cr}$ , which are the fracture energies for fibre tension, fibre compression, matrix tension and matrix compression failure modes, respectively, which correspond to the area under the plot of Figure 2.5 for each one of the modes when the material is fully degraded.

The behaviour of cohesive zones used to model bonded interfaces is defined by an elastic constitutive matrix that relates the normal and shear stresses to the normal and shear displacements in terms of traction-separation laws that assume a linearly elastic behaviour followed by the initiation and evolution of damage. When a initiation criterion is met, material damage occurs following a damage evolution law defined by the user. A maximum nominal stress criterion (MAXS) will be used in the scope of this work to define the initiation of cohesive damage, which is given by

$$\max \left\{ \frac{t_n}{t_n^0}, \frac{t_s}{t_s^0}, \frac{t_t}{t_t^0} \right\} = 1, \quad (2.22)$$

where  $t_n$ ,  $t_s$  and  $t_t$  are the three components of the nominal traction stress vector and the subscripts  $n$ ,  $s$  and  $t$  denote the normal and two shear tractions, respectively. The stress values  $t_n^o$ ,  $t_s^o$  and  $t_t^o$  represent the maximum values of the nominal stress when the deformation is applied normal to the interface or in the first and second shear directions, respectively.

Damage growth is defined by the rate of stiffness degradation which is expressed in the form of a damage evolution law. In this work, the damage evolution law given by the Benzeggagh-Kenane (BK) criterion will be considered, which is based on the dependence of the fracture energy on the damage made and takes the the following form,

$$G_n^{cr} + (G_s^{cr} - G_n^{cr}) \left\{ \frac{G_S}{G_T} \right\}^\eta = G^C, \quad (2.23)$$

where

$$\begin{cases} G_S = G_s + G_t, \\ G_T = G_n + G_S. \end{cases} \quad (2.24)$$

$G_n^{cr}$ ,  $G_s^{cr}$  and  $G_t^{cr}$  are the critical fracture energies values in modes I, II and III, respectively, which are predicted by the fracture mechanics theory with respect to the three modes of failure to propagate in a material due to tensile and shear stresses (see Figure 2.6).  $G_n$ ,  $G_s$  and  $G_t$  refer to the work done by the traction and its conjugate relative displacement in the normal, first and second shear directions, respectively.  $\eta$  is a material parameter and  $G^C$  is the mixed-mode fracture energy. It is important to note that this criterion is particularly useful when  $G_s^{cr} = G_t^{cr}$  [27].

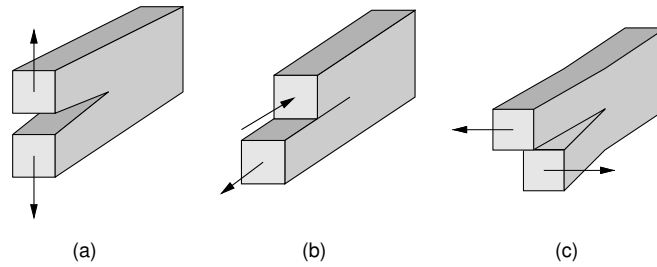


Figure 2.6: Fracture growth modes: (a) Mode I (opening/peeling); (b) Mode II (sliding); (c) Mode III (tearing) [34].

## 2.2.4 Applications in the aerospace industry

The development of improved materials for aerospace applications is based on balancing the weight savings through increased specific strength or stiffness against affordability [4]. Fibre-reinforced composites provide improvements over conventional metal alloys regarding their specific properties and density. Carbon fibres present mechanical properties that vary with the type of carbon fibre, but overall present have high specific stiffness and strength when compared to other materials, thus being extensively used for aerospace applications.

The implementation of composite materials in aerospace structural elements for reducing weight without compromising the life-cycle and costs of the materials, led to a series of studies on the fundamental understanding of their properties and mechanical behaviour. The project POSICOSS (Improved Postbuckling Simulation for Design of Fibre Composite Stiffened Fuselage Structures) [35] and the follow-up project COCOMAT (Improved Material Exploitation at Safe Design of Composite Airframe Structures by Accurate Simulation of Collapse) [18] were supported by the European Commission to develop improved analysis tools, validated by new experimental data bases for curved stringer-stiffened carbon fibre-reinforced polymer (CFRP) panels of future fuselage structures. COCOMAT used the reliable and fast procedures for post-buckling analysis and design provided by the POSICOSS project, analysing and improving the existing tools and taking stringer separation and material degradation into account. This was made in order to provide recommendations for buckling, post-buckling and collapse analysis of thin-walled aerospace structures. The COCOMAT team used simple stress-based failure criteria which did not present a realistic prediction of failure. Pereira [19] studied alternative damage models for the thin-walled stiffened CFRP panels with T-shaped stringers used in the COCOMAT project and evaluated the influence of stringer geometry on the behaviour of the panels under axial compression in order to find the design with the best structural efficiency. Silva [20] followed up the work presented by Pereira, doing a numerical investigation on the mechanical behaviour of the panels previously obtained subjected to high velocity impact loadings. This provided a better understanding on the influence of parameters such as ply orientation, stacking sequence, position of impact, angle of impact, mass and shape of the impactor on the panels' dynamic behaviour. Martins [21] further investigated the response of the panels under impact loading by considering projectiles of different materials (ice and steel) and geometries (spherical, cylindrical and conical) and the pre-loading of the structures. Additionally, the strain rate dependence of the material properties was incorporated into the numerical model.

### **2.3 Blast response of FRP panels**

The increasing use of FRP laminate composites in light-weight structures with risk of experiencing explosive blasts led to their research in order to model and predict the dynamic behaviour and crashworthiness of composite structural elements under explosive blast loading. This section provides a review on the outcomes of experimental and numerical investigations on the dynamic response of FRP laminates and influence of material and blast parameters on the deflection, strength and blast-induced brittle damage processes of plane and curved panels.

Analytical models have been proposed in order to obtain the deformation and vibration response of FRP laminates for different boundary conditions [12]. The main drawback that the majority of the models present is the fact that strain rate dependent properties of FRP laminates have not been applied to predict the blast response and, in most cases, their predictive accuracy has not been validated using experimental data [12]. Experimental testing has been performed to gather information on the blast response of FRP panels, however, it is difficult to compare results as no standard test is used to assess blast behaviour of materials. Finite element (FE) models using commercial FE software such

as Abaqus/Explicit, overcome some of the difficulties of conducting experimental tests and were found to predict with accuracy the blast-induced deformation and the initiation and evolution of damage within FRP laminates. Blast models and experimental tests have been used to assess the influence of blast and material parameters such as the scaled distance of the explosive charge [13, 14], the thickness-to-area ratio of the laminate [15], the fibre type [13, 14] and ply orientation [15] on the blast response of composite structures. However, while the majority of blast studies on FRP laminates have been performed on flat panels [12–15], fewer studies take into account the effects of curvature into blast damage resistance [16, 17].

As the shock wave impinges a panel, it will initially deflect in the wave direction due to the loading from the shock wave and the deformation continues due to inertia. The impulse measures the energy transferred to the panel and highly influences the dynamic response and amount of deflection created. Gargano et al. [14] reported that under low impulse conditions, laminated panels elastically deform and then regain the original position, where multiple elastic vibrations can occur depending on the damping properties of the material and boundary conditions. For high blast impulses, laminates suffer irreversible deformations due to blast-induced damage. Figure 2.7 (a) shows the centre-point deflection-time history response of a flat FRP panel subjected to low and high shock wave impulses. It is observed that the centre-point will reach a maximum out-of-plane deflection and deflects back partially or completely depending on the amount of damage. Additionally, the maximum deflection of laminates will increase linearly with the impulse of the shock wave up to a maximum value of impulse where damage initiates and result in non-linear effects in the deflection of the panels, as seen in Figure 2.7 (b).

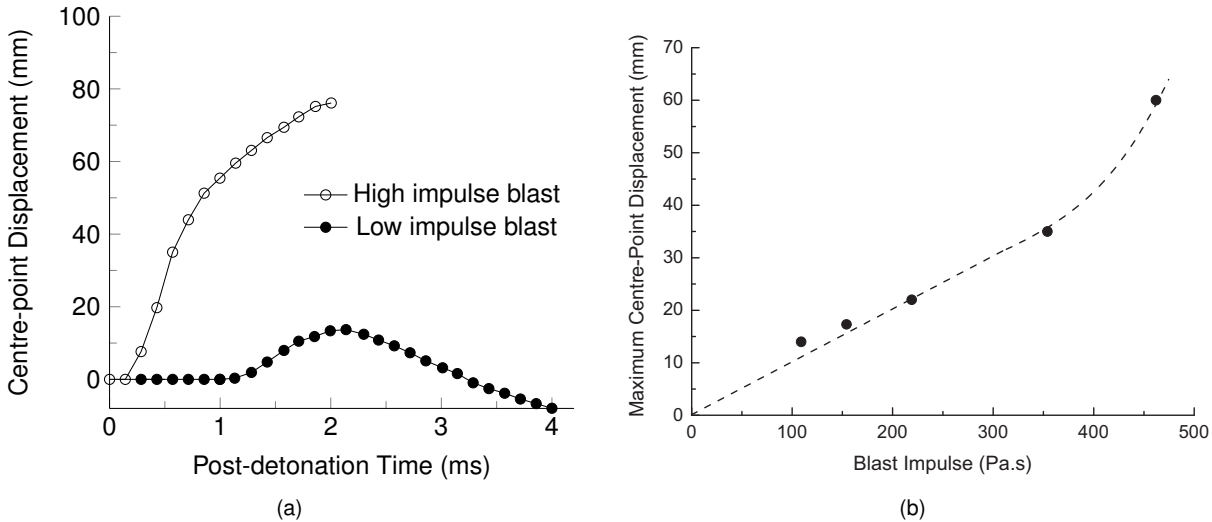


Figure 2.7: (a) Maximum deflection-time history and (b) effect of blast impulse on the maximum deflection of a CFRP laminate [12].

The shock effect originated by the reflected pressure built up when a blast wave impacts a panel results in a compressive stress wave that travels through the thickness of the laminate, which can result in the initiation of damage on the matrix and fibres. When reaching a free surface, the stress wave is reflected, originating a tensile wave that travels in the opposite direction, what can lead to inter-laminar damage in the form of delamination, since the tensile wave originates a mode I fracture growth between

adjacent fibre layers [22].

In the experimental investigation of Tekalur et al. [36], the difference in the load required to initiate damage and to cause complete failure in CFRP laminates was found to be small, due to the brittle nature and low failure strain of the material. Figure 2.8 (a) shows the damage progression on the incident surface of a woven carbon fibre/vinyl ester composite panel subjected to a controlled blast loading using a shock tube. The panels resisted damage until a certain value of pressure (around 0.6 MPa). Above this value, known as threshold pressure level, extensive levels of delamination and fibre rupture were observed.

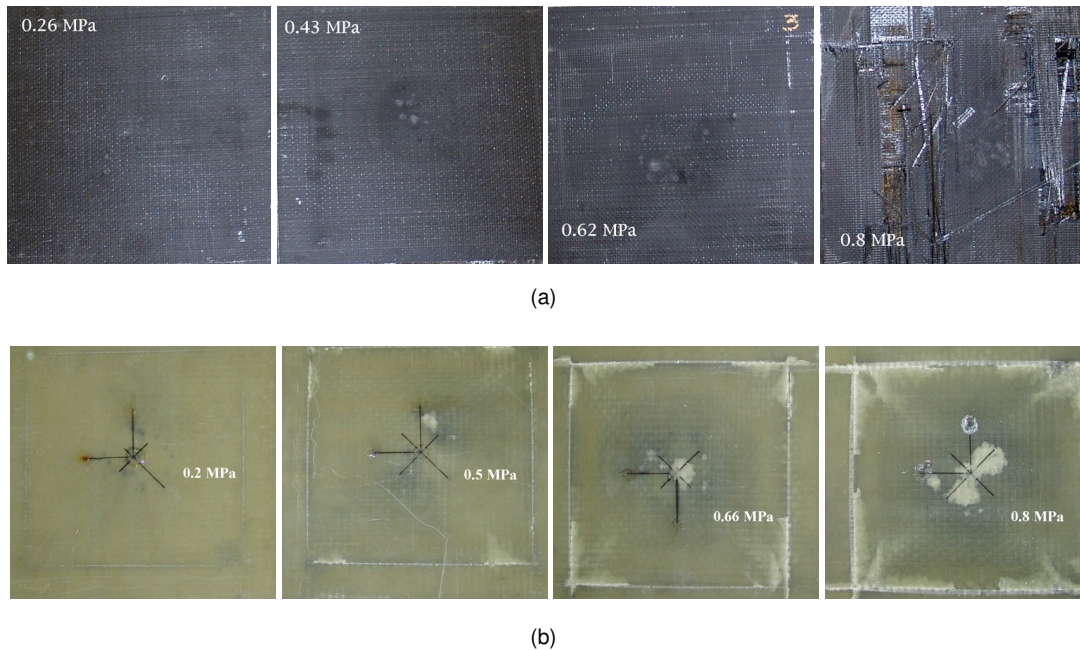


Figure 2.8: Damage progression on the (a) carbon and (b) glass FRP panels for increasing pressure loading values [36].

Gargano et al. [13] also investigated the blast-induced damage on flat woven FRP laminates using electron microscopy and ultrasound in order to assess the types and extent of the damage modes on the panels for a range of blast impulses. The different damage modes observed in the laminates were found to follow a sequence of initiation and development influenced by increasing shock wave impulses. Intra-laminar failure (or ply failure) first occurred in the form of fibre/matrix interfacial cracks and matrix cracks, increasing in length and volumetric density for higher blast intensities. For higher shock wave impulses, the fibres experienced kinking/micro-buckling and rupture due to compressive and tensile stresses, respectively, and inter-laminar failure occurred in the form of delamination. The amount of damage increased with increasing blast wave loading until the laminate suffered complete rupture. A FE model later developed by Gargano et al. [14] was found to predict with reasonable accuracy the ply rupture and delamination under high impulse blasts using Hashin failure criteria and damage criteria for cohesive surfaces between plies, respectively.

Experimental tests were conducted by Kumar et al. [16] in order to understand the effect of plate curvature on the blast resistance properties of convex FRP laminate panels. In the experiments, three

panels made of a CFRP laminate composite with different radii of curvature, i.e., infinite (Panel A), 305 mm (Panel B) and 112 mm (Panel C), were held under clamped boundary conditions on all the four edges during the loading from a planar shock wave propagating in a shock tube. Regarding the deflection of the panels, two different modes of deflection were identified, namely an indentation and a flexural mode. When subjected to blast loadings, the panels started to deflect in the indentation mode, identified by the localized nature of the deformation. As the displacement increased, having larger values in the center than in the edges, the flexural mode became dominant and a global overall deflection of the panel was observed. Similar observations were made in the works of Shen et al. [11] and Sinclair [17]. The deflection history of the cross-section of the panels studied by Kumar et al. [16] is presented in Figure 2.9, where both modes of deformation can be observed and a transition from the indentation to the global mode is seen for panels A and B.

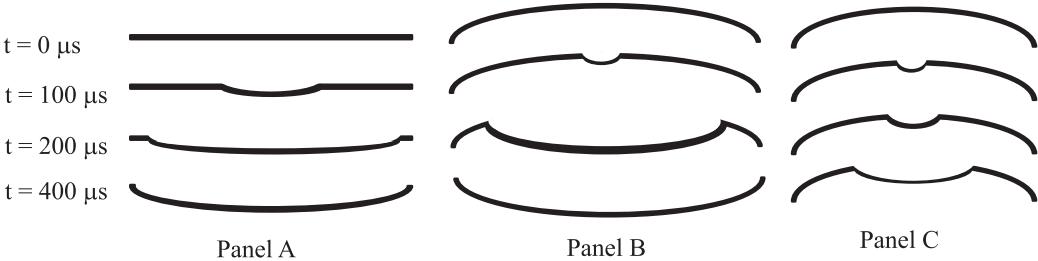


Figure 2.9: Deformation modes of CFRP laminate panels with different radii of curvature [16].

Panel curvature was found to influence the blast response of the structure. Firstly, it has an effect on the deformation modes. The flexural deformation was found to increase whereas the indentation deformation decreases for increasing radii of curvature. Additionally, the curvature changes the angle of incidence and reflected pressure of the blast wave. As the radius of curvature reduces to a limiting value, the effect of the shock wave loading decreases, as less energy is transferred to the panel [8]. As such, the panel with greatest curvature was found to withstand the least deflection during the blast event, as seen in Figure 2.10.

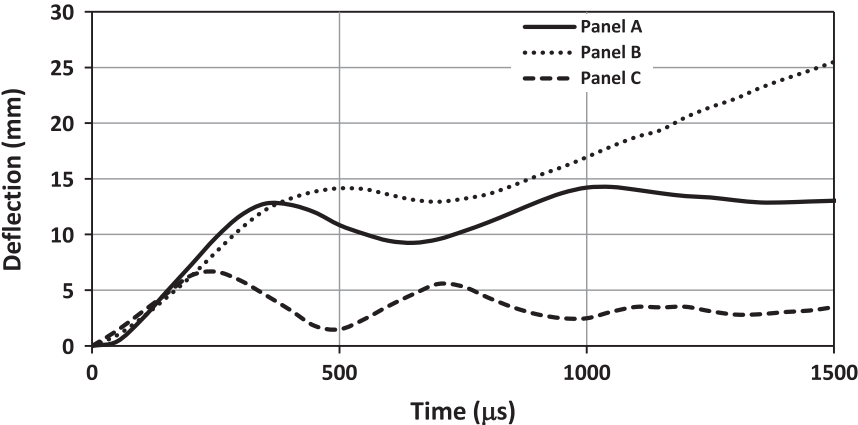


Figure 2.10: Centre point deflection history of CFRP laminate panels with different radii of curvature [16].

Furqan et al. [37] numerically investigated the influence of the incident surface configuration on the structural response of aluminium panels. Various shapes of panels were considered (i.e., flat, concave and convex) and subjected to the blast loading from an explosive charge with varying mass and stand-off distance. The results show that the concave panel exhibits a better structural response than the convex panel. This is due to the fact that, for the convex configuration, the panel bears more impact loading at the central point of the panel and therefore shows higher displacements at that point. On the other hand, the concave model shows a significant reduction of peak central node displacement (up to 67%) when compared to a flat panel.

It is important to note that, in the study carried out by Furkan et al. [37], the structural responses for each panel configuration were evaluated based exclusively in terms of peak displacement and velocity values. Moreover, the elastic brittle behaviour typical of FRP laminates under blast loadings enforces an analysis on the damage mechanisms of the composites. Therefore, further research is required to fully assess the curvature dependence of the blast response in the case of FRP laminates and the results found can not directly be applied to CFRP panels.

Laminate parameters such as fibre type [13, 14, 36], ply sequence, ply orientation and thickness [15] of the material have been studied to maximize the energy absorption, increasing structural resistance and to reduce the dynamic deformation and damage development. Gargano et al. [13] compared the damage on laminates reinforced with the same volume fraction of carbon and glass fibres under the same blast conditions. The glass fibre-reinforced composites present a more progressive failure for increasing shock wave loading conditions, whereas the carbon fibre-reinforced materials experience a sudden failure, which is in agreement with the results reported by Tekalur et al. [36] (see Figure 2.8). Additionally, it was found that CFRP laminates experience more damage due to delamination and fibre fracture over the range of blast impulses than their glass fibre counterparts (see Figure 2.11).

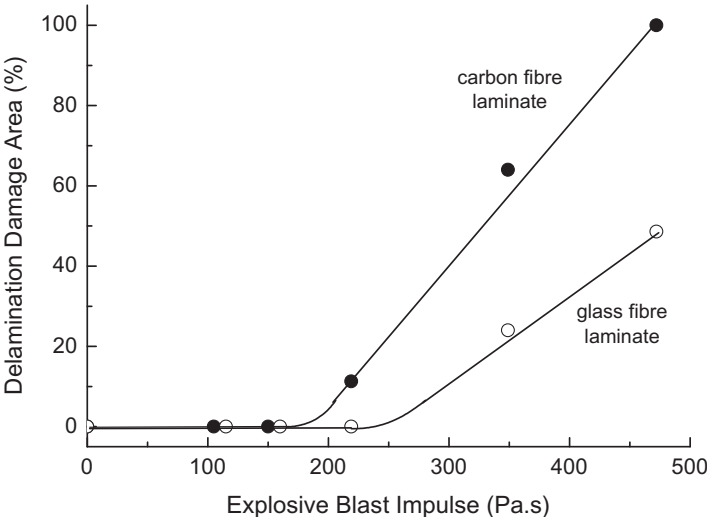


Figure 2.11: Delamination damage area with increasing blast impulses for carbon and glass fibre laminates [12].

These observations differ from the results obtained by Tekalur et al. [36], in which the fibreglass laminates were found to have a lower threshold pressure (around 0.2 MPa) than the carbon fibre coun-

terparts (seen Figure 2.8). Gargano et al. [13] attributed the difference in the blast performance of carbon fibres over glass fibre composites to the lower failure strain values of the carbon fibres, despite presenting higher tensile strengths. As stated previously, there are various types of carbon fibres with different specific properties and further research is needed to fully assess the influence of a wide range of fibre types on blast performance. Another consideration is that the panels studied by Gargano et al. [13] were simply-supported, whereas in the study of Tekalur et al. [36], the panels were fixed on all ends using a rigid clamping fixture.

The boundary conditions have a major influence on the dynamic response and failure modes of FRP composite laminates. Comotois et al. [38] investigated the blast response of (carbon and glass fibre) laminate panels subjected to the blast wave resulted from the detonation of a charge of PE4 for soft (i.e., adhesive bonded) and more rigid (i.e., clamped) boundary conditions. Damage in the form of delamination and ply rupture was found to be localised in the adhesively bonded region and more widely distributed when the panels were clamped, as schematically shown in Figure 2.12. This highlights the fact that the use of rigid boundary conditions in blast testing may result in damage distributions that are not representative of failure in larger structures [38].

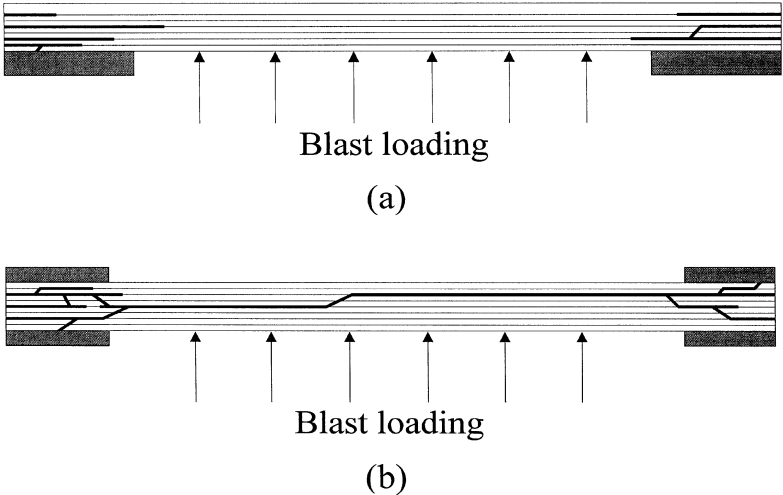


Figure 2.12: Schematic representation of the blast-induced delamination in FRP panels with (a) bounded and (b) clamped boundary conditions [38].

Numerical modelling of quasi-isotropic CFRP laminates by Batra and Hassan [15] shows that the energy absorption and blast damage depend on the  $[0/+45/-45/90]$  ply sequence (see Figure 2.13). The fibre orientation influences the time and location of each failure mode initiation and its direction of propagation. It was observed that in each case, the failure mode that first initiated caused the maximum energy dissipation (except in the case of delamination), and was dependent on the stacking pattern of the plies. The failure modes can be delayed by placing the  $45^\circ$  plies at the bottom of the laminate to resist fibre fracture, and the  $0^\circ$  or  $90^\circ$  plies at the top to resist delamination, as the energy dissipated due to matrix cracking is very small by comparison. The maximum deflections of the central point of the laminates were larger for the  $[0/+45/-45/90]$  and  $[0/-45/+45/90]$  laminates.



Varying the thickness of each ply was also found to have an influence on the maximum deformation and energy dissipation properties of the panels. The maximum deflection in the center point decays exponentially with an increase in the target thickness. Meanwhile, the target thickness determines the dominant failure mode and the energy dissipated due to delamination failure is maximum for the lower thickness.

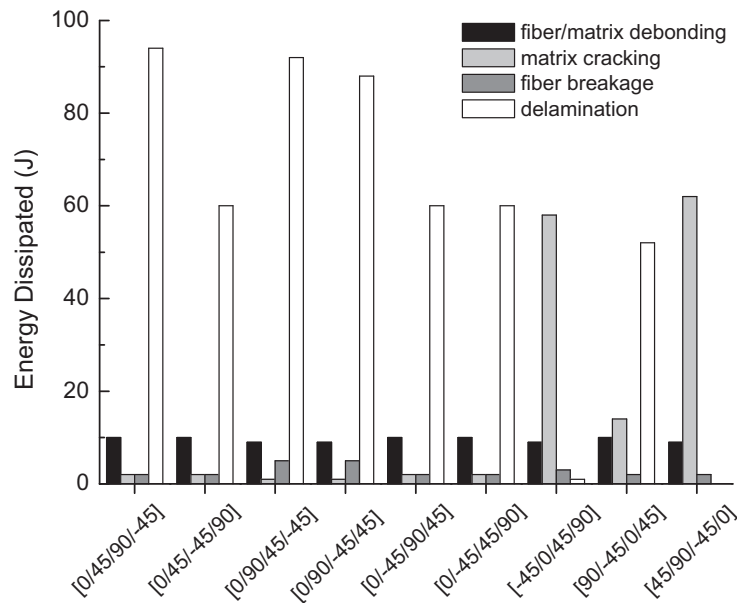


Figure 2.13: Influence of ply orientation on the energy dissipated by the failure modes [12].

The advantages of structural stiffeners in plates are unanimously recognized from a mechanical and economical standpoint [39]. Experimental investigations on stiffened curved CFRP panels understood as real parts of aircraft fuselages have been previously made during the project POSICOSS [35] and COCOMAT [18], which addressed the linear buckling and ultimate strength of CFRP single-curved panels. Under blast loadings, however, the research on the mechanical behaviour and influence of stiffeners on the dynamic response of panels is still very limited and, at the time of writing this work, no results regarding the blast response of CFRP reinforced curved panels is available in the literature.

The published research presented in this section provides a thorough comprehension on the effects of the blast phenomenon on the dynamic response of FRP flat panels. As stated, material properties such as thickness, fibre type and ply orientation have an effect on the blast resistance of the laminates. Furthermore, the prospect of providing an additional stiffness against explosive blasts through curvature and reinforcements on the panels requires further research, particularly of numerical nature, in order to deepen and complement the understanding of the influence of these parameters. Hence, this work will focus on a numerical analysis of the influence of the curvature and reinforcements (with different cross-section geometries) on the dynamic response of CFRP single-curved panels to the loading from an explosive shock wave.



# Chapter 3

## Numerical model

This chapter presents a description of the creation of a numerical model capable of simulating the blast response of a CFRP panel representative of a fuselage section of a new generation of commercial aircraft. The first section includes the approaches used into modelling the panels (which include the geometry, mesh and material properties), followed by a description of the boundary conditions and blast modelling. An approach to take into account the strain rate dependence of the materials under blast loading is also considered. Finally, in the second section, a numerical model is validated against experimental data.

The Explicit solver of finite element analysis (FEA) software Abaqus (version 6.14) was used for the simulations.

### 3.1 Description of the model

#### 3.1.1 Geometry

The panels studied in this research consist of variations of the reference panel designed in the COCOMAT project [18] and later replicated in the works of Pereira [19], Silva [20] and Martins [21], shown in Figure 3.1.

The reference panel incorporates five evenly-spaced T-shaped longitudinal stringers bonded to a cylindrical skin by an adhesive layer. Depending on the purpose of the analysis, variations of this panel were modeled. The geometric data of the (reference) panel is shown in Table 3.1.

The skin and stringers of the panels are made of the same unidirectional fibre-reinforced laminae, each with the same thickness,  $t$ , of 0.125 mm, giving the skin, the stringers' flange and web a total thickness of 1, 1.5 and 3 mm, respectively. The plies are stacked in various orientations, with the stacking sequences mentioned in Table 3.1. In the stacking labeling, the subscript  $s$  means that the stacking sequence is symmetric with respect to the mid-plane of the referred laminate. Additionally, " $0_N$ " and " $(+45,-45)_N$ " gives an indication on the number ( $N$ ) of times a given orientation or sequence of orientations, respectively, is repeated.

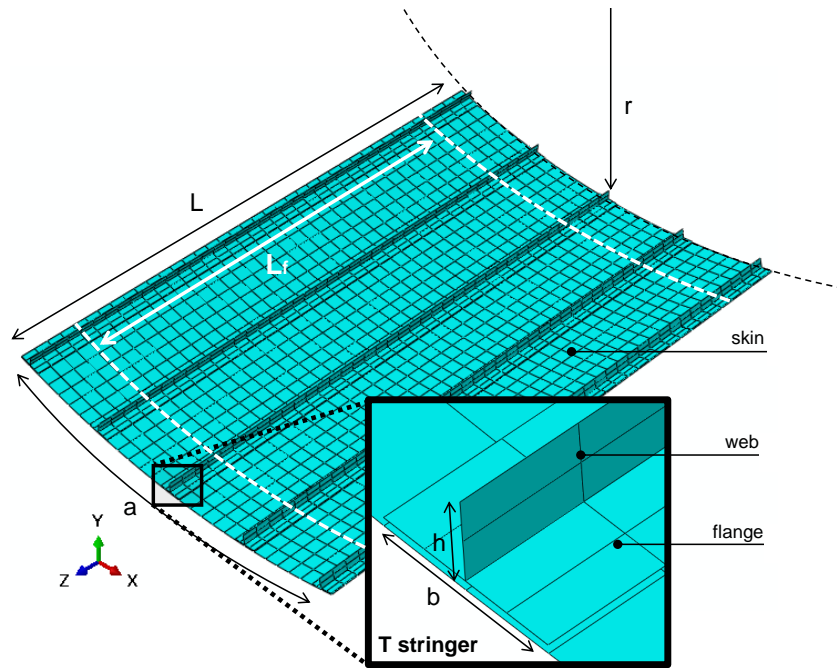


Figure 3.1: Geometry and mesh of the reference panel.

Table 3.1: Geometric data of the reference panel.

Dimensions		Composite layup	
Length (L) [mm]	780	Ply thickness (t) [mm]	0.125
Free length ( $L_f$ ) [mm]	660	Stacking sequence of the skin	$[90,+45,-45,0]_s$
Radius of curvature (r) [mm]	1000	Stacking sequence of the stringer flange	$[(+45,-45)_3,0_6]$
Arc length (a) [mm]	560	Stacking sequence of the stringer web	$[(+45,-45)_3,0_6]_s$
Stringer height (h) [mm]	14		
Stringer width (b) [mm]	32		

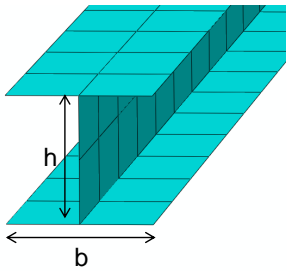
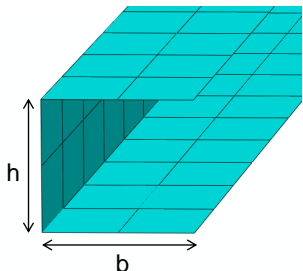
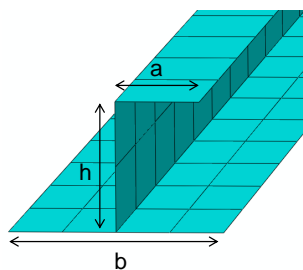
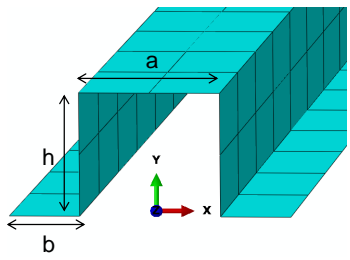
In order to study the influence of the curvature on the blast response of the CFRP panel, three models were considered. In this case, the panels consisted of only the skin (and, therefore, no reinforcements) with varying radius of curvature (500, 750 and 1000 mm). The remaining parameters follow the geometric data of the reference panel, given in Table 3.1.

To take into account the influence of reinforcements, stringers with four other cross-section geometries (I-, C-, J- and  $\Omega$ -shaped) were added into the model. The geometric data of the stringers' cross-section is listed in Table 3.2 .

For each geometry, the height of each web remained constant and equal to 14 mm as a way of maintaining the same usable space in an aircraft fuselage. At the same time, the dimensions of the flanges were defined so that the area of the cross-section, and consequently the structural weight of the stringers, was the same and equal to that of the reference T-shaped stringer.

The flanges and webs for each design have the same thickness as that of the T-shaped stringers, each one consisting on 12 and 24 plies of the unidirectional lamina used in the skin, respectively, with the exception of the  $\Omega$  configuration, in which the webs have the same stacking sequence (and therefore, the same thickness) as the flanges.

Table 3.2: Geometric data and mesh of the I-, C-, J- and  $\Omega$ -shaped stringers.

Shape	Cross-section geometry	Dimensions [mm]		
		a	b	h
I		—	16	14
C		—	16	14
J		9	23	14
$\Omega$		16	8	14

### 3.1.2 Mesh

The skin and stringers of the panels were discretized with 4-node shell elements (named S4 in Abaqus nomenclature [27]). Each node of the S4 elements has six degrees of freedom (DOF), consisting of a displacement and a rotation for each one of the three directions of the global coordinate system.

In Abaqus/Explicit, triangular and quadrilateral conventional shell elements are available in large and small-strain formulations. For most analyses, the standard large-strain shell elements are more appropriate, as large displacements invalidate the linearity governing the constitutive relations for small-strain conditions [27]. The use of quadrilateral elements results in an increment of the DOF in each element, achieving a higher accuracy, which motivated the choice of this type of element for the numerical model.

Additionally, a full integration option was chosen. Quadrilateral shell elements with reduced integration (namely, S4R) are available, in which the constitutive response of the individual element is computed by a single integration point. These elements, however, were found to introduce excessive constraints on the element's physical response due to hourglass control mechanisms without a significant improvement on the computational time of the simulations.

The mesh density was chosen upon a convergence analysis and four different meshes for the skin have been considered. The coarsest mesh had 70 elements whereas the finest had 4368. For each mesh, the skin was subjected to the blast loading from an explosive charge of 100g of TNT, located at 1m normally from the panel's centre point. The degree of accuracy of the mesh was analysed in terms of the normal displacement in the centre point of the panel for a given (always the same) time instant. For each mesh, the relative error ( $\Delta d_y$ ) of the normal displacement ( $d_y$ ) to the normal displacement for the finest mesh considered ( $d_y^{ref}$ ) was calculated, given by

$$\Delta d_y = \left| \frac{d_y - d_y^{ref}}{d_y^{ref}} \right|. \quad (3.1)$$

Figure 3.2 shows the results of the mesh convergence study and mesh applied to the reference panel. The converged element size was estimated to be 20mm, which resulted in 1092 elements and 1160 nodes in the skin of the panel as shown in Figure 3.1.

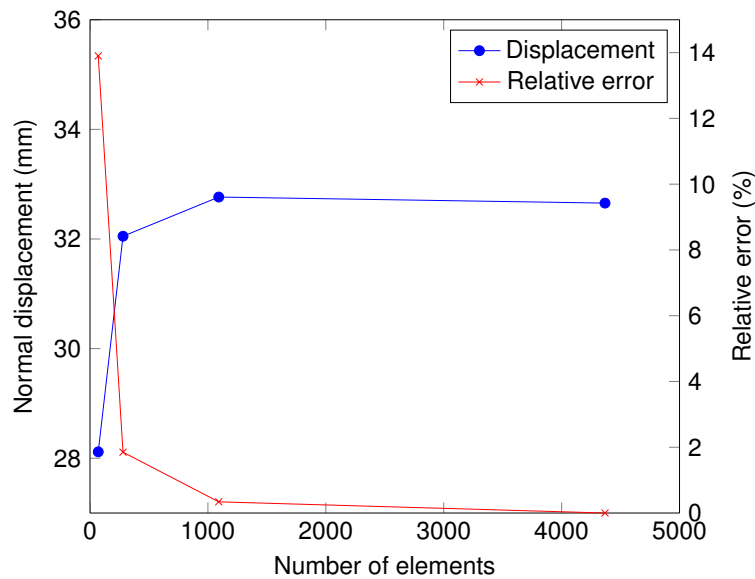


Figure 3.2: Mesh convergence study.

For the reinforcements, an individual mesh converge study was not made. It was assumed that the same mesh density and element type would present a similar level of accuracy for both cases, with and without stringers. The mesh of the stringers was chosen based on the contact modeling approach used on the interface between the skin and stringers. Contact pairs defined under the general contact option in Abaqus/Explicit use a master/slave contact algorithm in which the nodes on the slave surface cannot penetrate the segments that make the master surface. For that reason, the slave surface should be the

more refined one [27]. In the models, the surface of the stringers was selected as the slave surface and therefore presents a finer mesh. For the reference panel, the mesh of the T-shaped stringers was set to have 2 elements along the height of the web and 4 elements along the width of flange, making a total of 234 elements and 280 nodes for each stringer (Figure 3.1). The remaining configurations followed the same criteria, with the mesh densities for each design being represented in Table 3.2. The mesh of the surfaces of the flanges and webs comprise a total of 40 nodes along the longitudinal direction, the same as the mesh of the skin. The modelling of the adhesive interface using a contact approach is explained with more detail in the next section.

### 3.1.3 Materials

The unidirectional (UD) CFRP IM7/8552 (Carbon/Epoxy), used on the skin and stringers of the panel, and the adhesive Redux 312, which connects the skin and stringers, were chosen in view of their usage in the COCOMAT project and following works [18–21].

The IM7/8552 laminate is assumed to have an orthotropic elastic behaviour until failure. The material parameters necessary to define the lamina type material model in Abaqus, shown in Table 3.3, were obtained from the IM7/8552 material fabricated by Hexcel Composites [18]. Additionally to the four variables necessary to define an orthotropic material under plane stress conditions ( $E_1$ ,  $E_2$ ,  $\nu_{12}$  and  $G_{12}$ ), the lamina model includes the additional shear moduli  $G_{13}$  and  $G_{23}$  to take into account the transverse shear deformations in the shell type elements. The material properties are specified according to the material directions associated to an orthogonal local coordinate system with the 1-axis in the fibre direction, the 2-axis perpendicular to the fibres on the plane of the lamina and the 3-axis perpendicular to the plane of the lamina.

Intralaminar damage to the fibers and matrix was modelled using the Hashin failure initiation criterion for fibre-reinforced materials and the evolution of damage was implemented through a damage evolution law, described in detail in Section 2.2.3. In this work,  $\alpha$  was set to 1 in order to take into account the effect of shear on the fibre damage initiation. The parameters of the damage model shown in Table 3.3 include the tensile and compressive strengths (denoted by the subscript T and C, respectively) in the fibre and matrix directions (X and Y, respectively) and the fracture energies for each one of the failure modes, i.e., fibre tensile, fibre compressive, matrix tensile and matrix compressive ( $G_{ft}^{cr}$ ,  $G_{fc}^{cr}$ ,  $G_{mt}^{cr}$  and  $G_{mc}^{cr}$ , respectively).

Table 3.3: Material parameters for the CFRP IM7/8552 lamina [18, 40, 41].

Mass density		Elastic properties		Strength parameters		Fracture energies	
$\rho$ [kg/m <sup>3</sup> ]	1570	$E_1$ [MPa]	147000	$X_T$ [MPa]	2715	$G_{ft}^{cr}$ [N/m]	81500
		$E_2$ [MPa]	11800	$X_C$ [MPa]	1400	$G_{fc}^{cr}$ [N/m]	106300
		$\nu_{12}$ [-]	0.34	$Y_T$ [MPa]	56	$G_{mt}^{cr}$ [N/m]	277
		$G_{12}$ [MPa]	6000	$Y_C$ [MPa]	25	$G_{mc}^{cr}$ [N/m]	788
		$G_{13}$ [MPa]	6000	$S_L$ [MPa]	101		
		$G_{23}$ [MPa]	4000	$S_T$ [MPa]	131		

The laminate is modelled by creating a composite layup which assigns the orientation of the fibers, the material properties and the thickness within each ply of the composite. The orientation of the fibres within a ply is defined by the layup orientation, which is the reference orientation of all plies in the layup, and an additional relative rotation.

In the layup orientation, the primary axis was set to be aligned with the longitudinal direction of each part and the normal axis was set to be the normal to each surface, in which  $1 \equiv Z$ ,  $2 \equiv X$  and  $3 \equiv Y$  for the skin and stringer’s flanges and  $1 \equiv Z$ ,  $2 \equiv Y$  and  $3 \equiv X$  for the stringer’s webs (with the global coordinate system (X, Y and Z) represented in Figure 3.1). The model for each of the three composite layups used is shown in Figure 3.3.

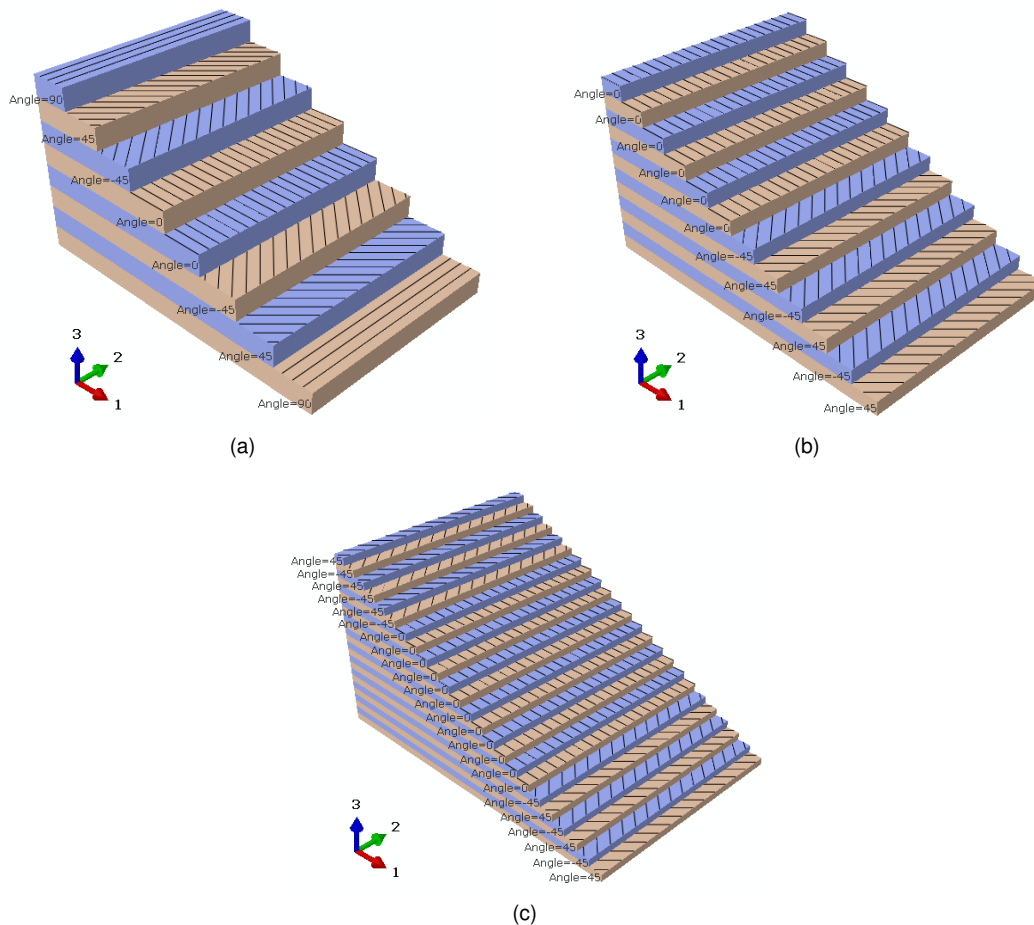


Figure 3.3: Composite layups: (a)  $[90, +45, -45, 0]_s$ , (b)  $[(45,-45)_3, 0_6]$  and (c)  $[(45,-45)_3, 0_6]_s$ .

The adhesive Redux 321, also manufactured by Hexcel Composites, was modelled using a cohesive contact behaviour. A cohesive contact approach can be used as an alternative to cohesive elements when modelling interface behavior. Both approaches follow the formulae and laws that govern cohesive constitutive behavior, including the linear elastic traction-separation model, damage initiation criteria and damage evolution laws described in Section 2.2.3. This choice was based on the fact that the blast loading of the CONWEP type is exclusive to shell, continuum and membrane elements and, therefore, cohesive elements are unable to capture the bonded interface and failure modes as a result of the explosive blast.



The cohesive interface is defined as part of the surface interaction property in Abaqus and takes into account both normal and shear forces in the adhesive layer. The interaction properties include the normal, shear and tangential stiffness coefficients associated with the bonded surfaces ( $K_{nn}$ ,  $K_{ss}$  and  $K_{tt}$ , respectively) and cohesive damage parameters.

The thickness of the adhesive layer cannot be introduced as a variable in the cohesive contact model and, therefore, the stiffness coefficients were obtained by dividing the material stiffness ( $E_{nn} = 3000$  MPa,  $E_{ss} = 1071$  MPa and  $E_{tt} = 1071$  MPa) by the thickness of the adhesive ( $t_a = 0.2$  mm), in order to account for the original thickness of the adhesive layer.

The maximum nominal stress criterion was used to predict the initiation of cohesive damage in the adhesive, which is defined by the maximum values of the normal and shear stresses in the cohesive interface ( $t_n^0$ ,  $t_s^0$  and  $t_t^0$ ). The Benzeggagh-Kenane (BK) criterion was used as a damage evolution law with a power coefficient of 4.5, which has been previously used for modelling adhesive failure in composite fuselage structures [42]. The damage evolution is defined by the critical fracture energies in mode I, II and III ( $G_n^{cr}$ ,  $G_s^{cr}$  and  $G_t^{cr}$ , respectively). Table 3.4 shows the cohesive properties for the adhesive model.

Table 3.4: Cohesive properties for the adhesive Redux 312 [18, 19].

Stiffness		Maximum stress		Fracture energies	
$K_{nn}$ [MPa/mm]	15000	$t_n^0$ [MPa]	8.3	$G_n^{cr}$ [N/m]	200
$K_{ss}$ [MPa/mm]	5355	$t_s^0$ [MPa]	38	$G_s^{cr}$ [N/m]	1000
$K_{tt}$ [MPa/mm]	5355	$t_t^0$ [MPa]	38	$G_t^{cr}$ [N/m]	1000

### 3.1.4 Strain rate

An important consideration in blast modelling is the strain rate ( $\dot{\epsilon}$ ) sensitivity of the composite material. Often models do not take into consideration the effects of strain rate on the elastic properties of FRP laminates, as the dependence of the mechanical properties at elevated strain rates is unavailable for newly developed composites. However, studies have found changes in the material properties that include tensile, compressive and in-plane shear fracture toughness of laminates by up to 50%, depending on the material used and strain rates induced by blast loading, which are typically in the range of 100-1000 s<sup>-1</sup> [13].

Constitutive models which account for the full orthotropic behaviour of laminated composites and the strain rate sensitivity on the response of the material under dynamic loads have been formulated [43]. The major shortcoming of the composite model used in this work is that the default lamina-type material model incorporated in Abaqus does not allow to specify the strain rate effects on the material properties of the CFRP laminate. In order to overcome this issue and qualitatively capture the influence of the strain rates induced during a blast event, the upcoming approach (equivalent to the one used in the work of Martins [21]) was followed:

- Firstly, the material property values at a quasi-static strain rate were used to model the panels,

which were then subjected to a blast loading. For each simulation, the nodal values of the components of the strain rate  $ER_{ij}$  tensor in the longitudinal and transverse directions were used to get a unified value for the in-plane strain rate, calculated as the modulus of the sum of two vectors. A time domain from the time of arrival of the shock wave up to the initiation of damage of the first failure mode according to the Hashin criterion was considered, capturing the time period in which the pressure loading is maximum. Then, an average value of the strain rate in the panel was obtained, in which the null values were disregarded.

- Secondly, the material properties at the average strain rate were calculated using Equations (3.2) and (3.3).
- Finally, a new model was created with the strain-dependent values of the material properties and subjected to the same blast conditions.

Schaefer et al. [44] studied the variation of the matrix-dominated properties of the composite material IM7/8552 at various strain rates. The average transverse and shear moduli ( $E_2$ ,  $G_{12}$ ) were normalized by their respective quasi-static values and were found to have an approximately linear dependence on the logarithm of the strain rate, given by the following relation,

$$E(\dot{\varepsilon}) = E(\dot{\varepsilon}_0) \left( m_e \log_{10} \frac{\dot{\varepsilon}}{\dot{\varepsilon}_0} + 1 \right), \quad (3.2)$$

where  $E$  is the modulus ( $E_2$ ,  $G_{12}$ ),  $m_e = 0.035$  is a constant and  $\dot{\varepsilon}_0 = 10^{-4} \text{s}^{-1}$  is the reference quasi-static strain rate.

A similar dependence was found for the transverse compressive ( $Y_C$ ), transverse tensile ( $Y_T$ ) and shear strength ( $S_L$ ), represented by

$$F(\dot{\varepsilon}) = F(\dot{\varepsilon}_0) \left( m_f \log_{10} \frac{\dot{\varepsilon}}{\dot{\varepsilon}_0} + 1 \right), \quad (3.3)$$

with  $F$  being the strength ( $Y_C$ ,  $Y_T$  and  $S_L$ ),  $m_f = 0.055$  a constant and  $\dot{\varepsilon}_0 = 10^{-4} \text{s}^{-1}$  the reference quasi-static strain rate.

For the blast conditions used in this work, the effect of strain rate was found to result in an improvement of the modulus and strength by up to about 17% and 26%, respectively.

### 3.1.5 Blast load modelling and boundary conditions

Pressure loading due to an incident shock wave caused by an in-air explosion is calculated using the CONWEP model. The CONWEP model implemented in the Abaqus/Explicit software was adopted for simulating the structural response analysis under blast loading in virtue of its accuracy and computational efficiency, especially for free-air (i.e., when there is no interference from reflective surfaces or shadowing objects) and far-field (i.e., when the effects of the dynamic pressure and explosive fireball can be disregarded) blast conditions [22].

As stated in Section 2.1.5, the shock wave overpressure profile is calculated using the empirical data obtained by Kingery and Bulmash [26] and implemented into CONWEP, which is capable of predicting the air blast conditions for a wide range of scaled distances [22]. The user-defined parameters that define the incident wave loading on structures include the equivalent mass of TNT, the spatial coordinates of the detonation point and the type of blast, which can be either ground surface or free-air detonation. The latter was used in the current work.

The shock wave overpressure-time profile has an exponential decay, following the relation given by the Friedlander equation (Equation (2.1)). When arriving at the contact surface, the CONWEP algorithm calculates the overpressure based on Equation (2.8), which is applied as a pressure load directly onto the surface.

The boundary conditions were set to approximate the constraints used in the previous studies involving these panels [19, 20, 40] and do not reflect the structural response of the panel when incorporated on the fuselage of an aircraft. Figure 3.4 shows the boundary conditions applied to the models. The edges of the panel marked with a black dashed line were clamped, with all 6 DOF restrained. The region marked in white, which corresponds to the first 60 mm from each end, only allowed axial and transverse displacement (in the Z and X-direction, respectively), with the remaining displacement and all rotations restricted. Finally, a length of 660 mm of the edges on each side of the panel (in red) was set free.

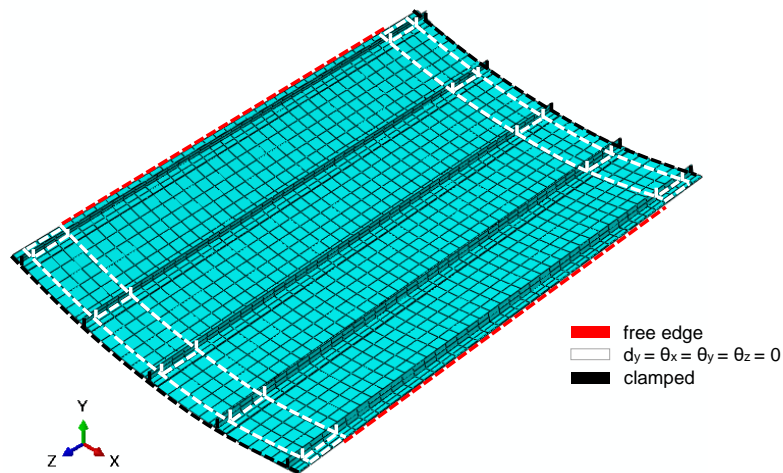


Figure 3.4: Boundary conditions.

## 3.2 Validation of the numerical model

Before the finite element model developed can be used to study and predict the response to blast loading of the panels, it lacks validation against experimental data. As no experimental data on the blast response of the panels studied in the scope of this work is available in the literature, the experimental and numerical investigations into the blast response of FRP laminates performed by Gargano et al. [13, 14] were used to validate the numerical model, as it follows similar modelling options as those used in this work, regarding blast conditions and material properties. The model's accuracy was

assessed by comparing the experimental results obtained regarding the out-of-plane deflection and resulting damage of CFRP laminates in near-field and far-field explosive blasts. Additionally, experimental data of the overpressure-time profile of the shock wave was used to validate the shock wave simulation using the CONWEP model.

The experimental setup used in the explosive testing of the panels performed by Gargano et al. [13] consisted of a flat laminate plate clamped in a vertical position within a steel window frame lined with soft rubber, allowing the plate to flex under the blast loading. The target plate geometry and boundary conditions were replicated as seen in Figure 3.5. Only the rotational DOF in x and y were allowed for the edges in the x-axis direction and y-axis direction, respectively. In all edges, the displacement in z was restrained. The material properties and laminate layup of the carbon-polyester laminate were defined as provided by Gargano et al. [14]. The plate was modeled as a shell with S4R elements, which were the same elements used in the numerical model of Gargano et al. [14], and the converged element size was found to be 4 mm, which resulted in 4761 elements and 4900 nodes in the target structure.

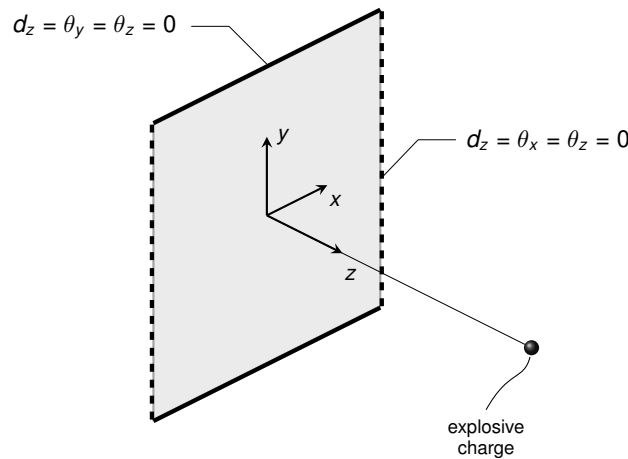


Figure 3.5: Schematic representation of the boundary conditions of the FEM.

The explosive charge was located in the horizontal plane of the centre of the plate, at the same height. Table 3.5 shows the experimental conditions used for the explosive blast testing, which were later replicated in terms of the explosive weight and stand-off distance.

Table 3.5: Experimental test conditions [14].

Explosive weight (PE4) [g]	Stand-off distance [m]	Field condition
100	1.0	Far-field
100	0.8	Far-field
100	0.6	Far-field
100	0.4	Near-field
160	0.4	Near-field

In the experimental tests, a charge of PE4 explosive was used, which has the same performance as C4 in terms of producing an air blast [25] and therefore, the relations shown in Section 2.1.2 for C4

were utilized in order to obtain the equivalent mass of TNT. The equivalent mass of TNT was calculated for each one of the test conditions and used in the CONWEP model to simulate the blast wave. The overpressure-time profiles in far-field conditions are presented in Figure 3.6. The numerical results are in good agreement with the experimental data, with the peak overpressure presenting differences between 1.43% and 4.80%. It is expected that, as the stand-off distance decreases, the overpressure values obtained using CONWEP become less accurate, given that it does not take into account the effects of the explosive fireball. For near-field conditions, the experimental measurement of the pressure decay was not possible due to the effect of the fireball on the readings of the pressure transducers [13].

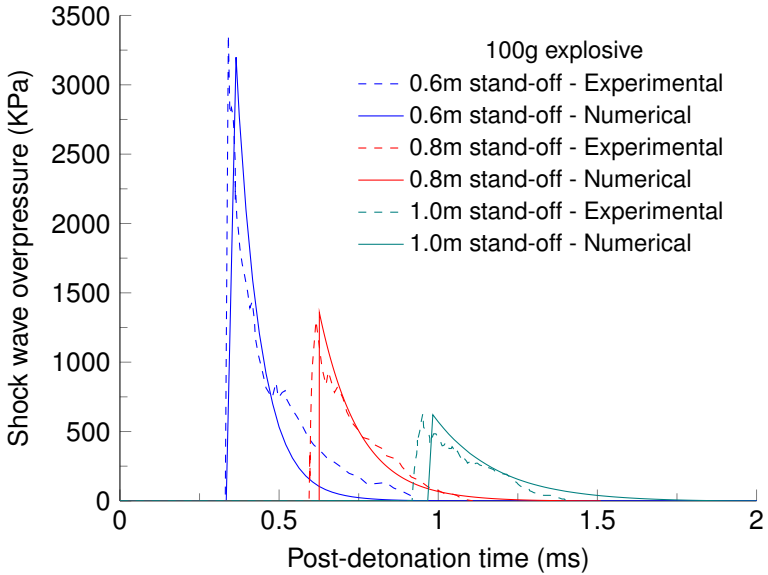


Figure 3.6: Far-field measured (dashed lines) and numerical (solid lines) overpressure-time profiles.

The model predicted with reasonable accuracy the deflection of the plate. When subjected to the explosive blast, the plate deflected in the same direction of the shock wave and then deflected in the opposite direction, depending on the blast impulse. Due to the symmetry regarding the boundary conditions and geometry of the target, the displacement was maximum at the centre point of the plate. The maximum center-point displacement history shows a good agreement for the initial deflection of the plate. After a certain instant, the agreement is poor, being increasingly less accurate for higher impulse levels. The omission of damping in the material properties of the system as well as the simplifications in the boundary conditions of the support structure (used to replicate the boundary conditions due to the steel window frame lined with soft rubber) causes a quicker response of the finite element model and a mismatch of the peak deflection.

The effect of the impulse on the maximum out-of-plane displacement of the plate is shown in Figure 3.7. As expected, for increasingly higher blast impulses, the displacement values also increase. The agreement between experimentally measured and numerical values of the maximum deflection are very good. For low blast impulses (i.e., in far field conditions), the FEM accurately predicts the impulses (with a maximum difference of 10%) for the same test conditions and the displacement follows a linear variation, with the maximum centre-point displacement presenting a variation within 11%. In near-field

conditions, however, CONWEP over-predicts the impulses generated by the shock wave, for the reasons stated previously, which leads to higher maximum out-of-plane displacements. Despite this, it is possible to observe that the displacements obtained by the FEM follow the trend that was expected regarding the displacement and therefore are in good agreement with experimental data.

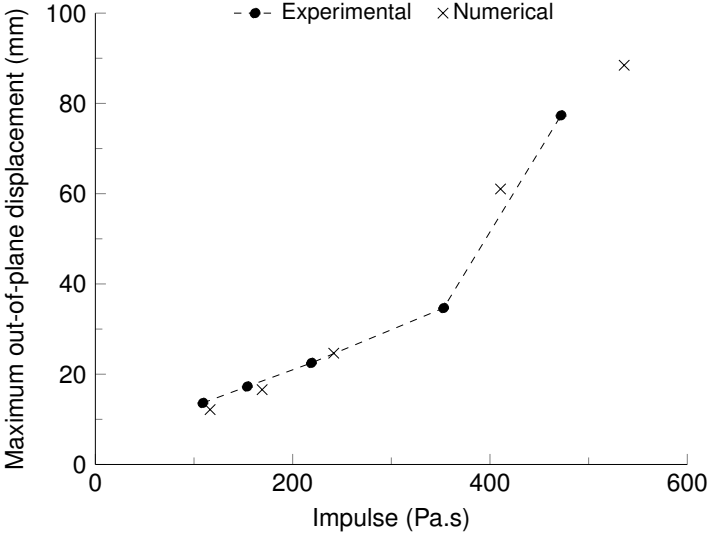


Figure 3.7: Effect of blast impulse on the maximum out-of-plane displacement.

Damage initiation was also modelled using Hashin’s damage initiation criteria, as described before. The FEM cannot predict delamination and no further discussion of delamination as a failure mode is thus carried in this work. The numerical model predicted the initiation of fibre kinking and matrix crushing at an impulse level of about 170 Pa.s. At around 240 Pa.s, the fibre rupture and matrix cracking initiate. The model predicted with accuracy the initiation of damage at several discrete regions in the plate edges, which rapidly propagated towards the centre. In the experimental and numerical investigations conducted by Gargano et al. [13, 14], rupture in the plies was observed for the highest blast impulses. In the models developed in this work, these cracks match with the elements in which the damage variables for all four failure modes (described in Section 2.2.3) reach unity and therefore the elements offer no resistance to further deformation and the output variable STATUS is set to zero, as seen in Figure 3.8.

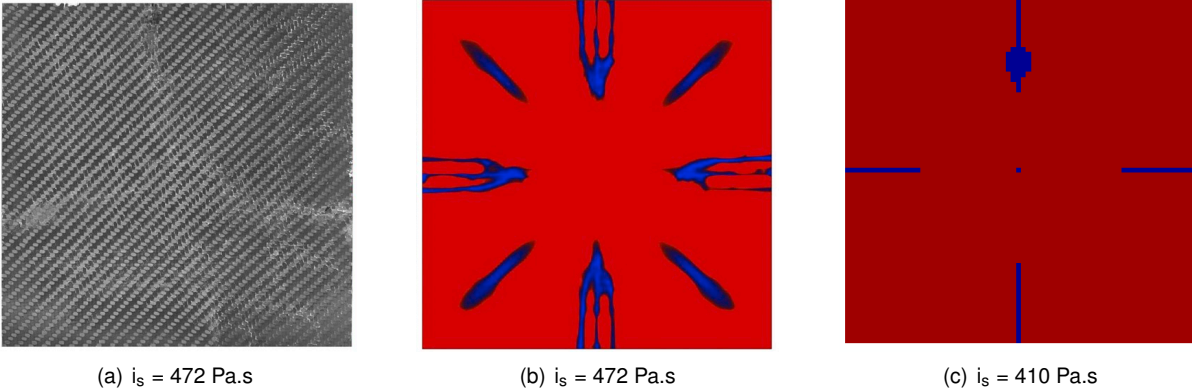


Figure 3.8: Ply rupture regions: (a) experimental [13], (b) numerical [14] and (c) numerically replicated.

Overall, the proposed numerical model successfully incorporates most of the key aspects of the deformation and failure mechanisms during the blast loading of a CFRP laminate under certain blast conditions, hence supporting the use of the methodology proposed in the study of composite structures subjected to explosive blast events.





# Chapter 4

## Results and discussion

In this chapter, the numerical results on the dynamic response of (stiffened and unstiffened) CFRP singly-curved panels subjected to blast loading are presented. The numerical study was carried out in order to examine:

- The dynamic response of the unstiffened reference panel due the shock wave loading applied on the concave and convex surface;
- The influence of the radius of curvature on the blast response of the panels;
- The effect of structural reinforcements with five different cross-section geometries (T-, I-, C-, J- and  $\Omega$ -shaped) on blast mitigation.

The data will be presented in terms of the deformation of the panels, an energy analysis and an assessment of the blast-induced damage on the plies of the laminate for identical far-field explosive blast loading conditions. These analyses seek to give a complete and detailed description of the blast response of singly-curved CFRP panels, representative of a fuselage section.

### 4.1 Dynamic response analysis

The dynamic response of the curved CFRP panel with the reference geometry and without reinforcements is firstly presented here. The panel was subjected to a shock wave originated by the explosive blast of a charge with a mass of TNT,  $W_e$ , of 100 g. The explosive charge was located at a stand-off distance, SOD, of 1 m, normal to the centre-point of both the concave and convex surfaces of the panel. These conditions were chosen in virtue of the observations made in Section 3.2, in which the CONWEP algorithm was found to simulate with accuracy the overpressure-time profiles of blast waves in far-field conditions, where the loading and thermal effects of the fireball due to the explosion can be disregarded and the loading that the structure experiences is limited to the effects of the shock wave.

The shock wave overpressure-time profile induced by CONWEP is given by the output variable IW-CONWEP in Abaqus [27] and is shown in Figure 4.1.

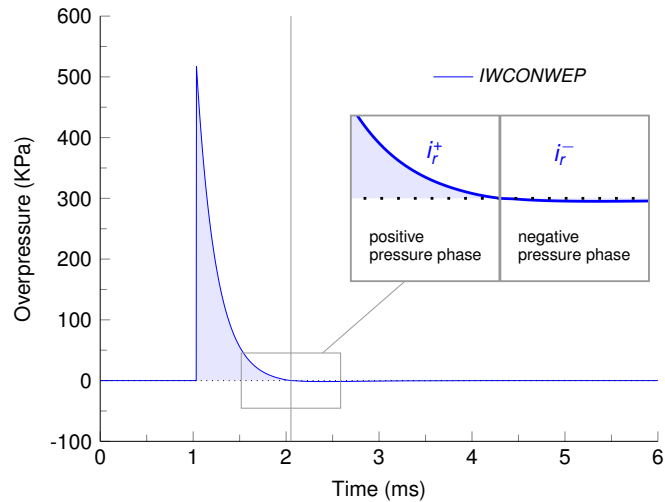


Figure 4.1: Overpressure time-history of free-air blast with  $W_e = 100$  g and SOD = 1 m measured in the centre-point of the panel.

Contrary to other empirical models, CONWEP takes into account both the positive and negative pressure phases of the overpressure-time curve. Under the blast conditions considered, the shock wave has a total impulse of approximately 106.70 Pa.s. When considering the impulse only due to the positive pressure phase of the overpressure-time curve, it can be estimated that the value shows a difference of only about 1.47% with respect to the total impulse. This supports the assumption that the negative pressure phase can be ignored when taking into account the dynamic loading due to a shock wave, as stated in Section 2.1.1 and, therefore, the loading from the negative pressure phase was disregarded in the analysis.

The contour plots of IWCONWEP during the blast loading event show a clear indication of the spherical propagation of the shock wave front. This resulted in distinct distributions of the load on the surfaces, depending whether the shock wave interacted with the concave or convex surface of the panel, as seen in Figure 4.2.

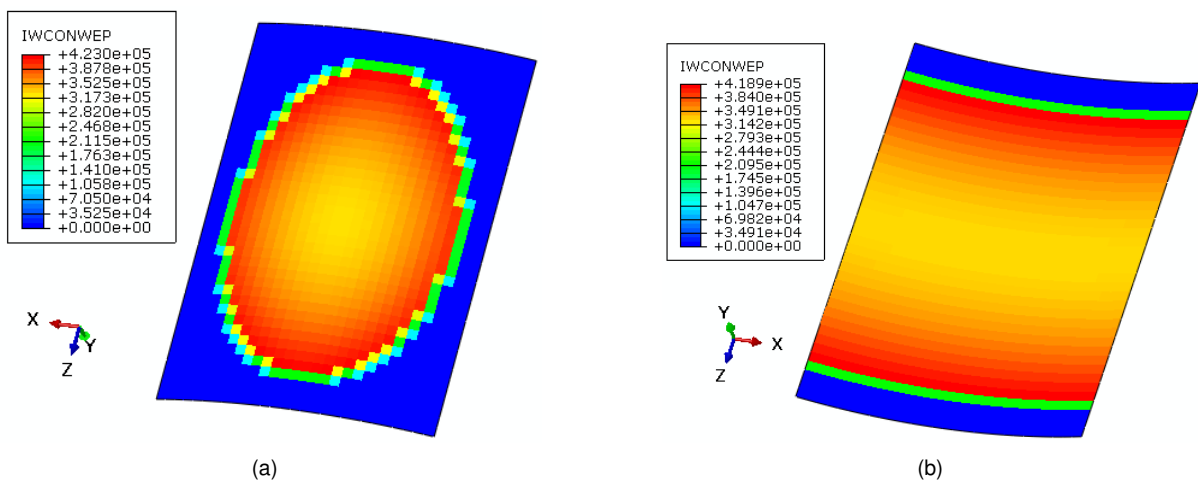


Figure 4.2: Distribution of the incident overpressure (in Pa) due to the shock wave in the (a) convex and (b) concave surfaces of the panel for the same post-detonation time instant ( $t=1.13$ ms).

For the convex configuration, the shock wave first interacts with the centre of the panel, progressively propagating towards the edges along the longitudinal and circumferential directions. Hence, two regions of response in the panel can be identified. First, the localised nature of the blast load results in a bounded deformation pattern in the form of indentation. This results in an increase of the deformation, which gives rise to high strains in the centre region of the panel in this very first part of the blast event. As the shock wave propagates spherically, the deformation progressively increases from the centre to the edges, and the indentation mode is replaced by a global response which comprises two deformation regimes in the form of bending and stretching in virtue of the out-of-plane loading and boundary conditions applied. These modes of deformation have been previously reported in experimental analyses found in the literature [11, 16, 17].

In the case of the concave specimen, however, the loading from the shock wave follows a different pattern. As it reaches the surface, the shock front acts on a "strip" along the curvature of the panel, propagating along the longitudinal axis. This results in higher out-of-plane displacements in the free edges of the panel and a more unidirectional distribution of the stresses along the surface. In this case, the indentation regime previously mentioned is not observed and the dynamic response of the panel will mainly comprise the two global modes of deformation, i.e., bending and stretching.

To give a clear insight on the deformation modes of the panel, the deflections along the longitudinal (Z-axis) and circumferential (X-axis) directions from the centre of the convex and concave surface during the shock wave impingement were considered to be representative of the deformation pattern of the panels and are, therefore, plotted in Figure 4.3. Note that, for both cases, the displacement is considered positive in the direction of propagation of the blast wave.

The blast wave starts to interact with the panel at around  $t = 1.04$  ms from detonation. From that point on, the symmetry of the deflection process about the centre of the panel is observed due to the symmetry of loading and boundary conditions, however, a very different deformation pattern is seen. For the same time instant, it is possible to observe that the displacement along the Z-axis is very similar for both cases. This is due to (i) the loading conditions along this path in both cases is the same and (ii) the panel presents similar stiffness despite configuration. The stiffness of the structure depends of the material properties and geometry. Although the geometry is the same, the concave configuration was found to withstand higher values of strain rate across the surface. This leads to an increase of the strength properties of the laminate which causes a slight decrease on the values of out-of-plane displacement for this case. This can be specially noticed when comparing Figure 4.3 (a) and (b), where the deformed shapes of the concave surface shows a lower curvature near the centre of the panel when compared to the convex configuration.

Along the X-axis, however, the deformation profiles show different shapes for the different configurations by virtue of the geometry of the incident surface in each case. The maximum out-of-plane displacement occurs at different points for each specimen. For the convex configuration, the centre-point of the panel presents the highest displacement, whereas in the concave case, the deflection is higher near the free edge of the panel.

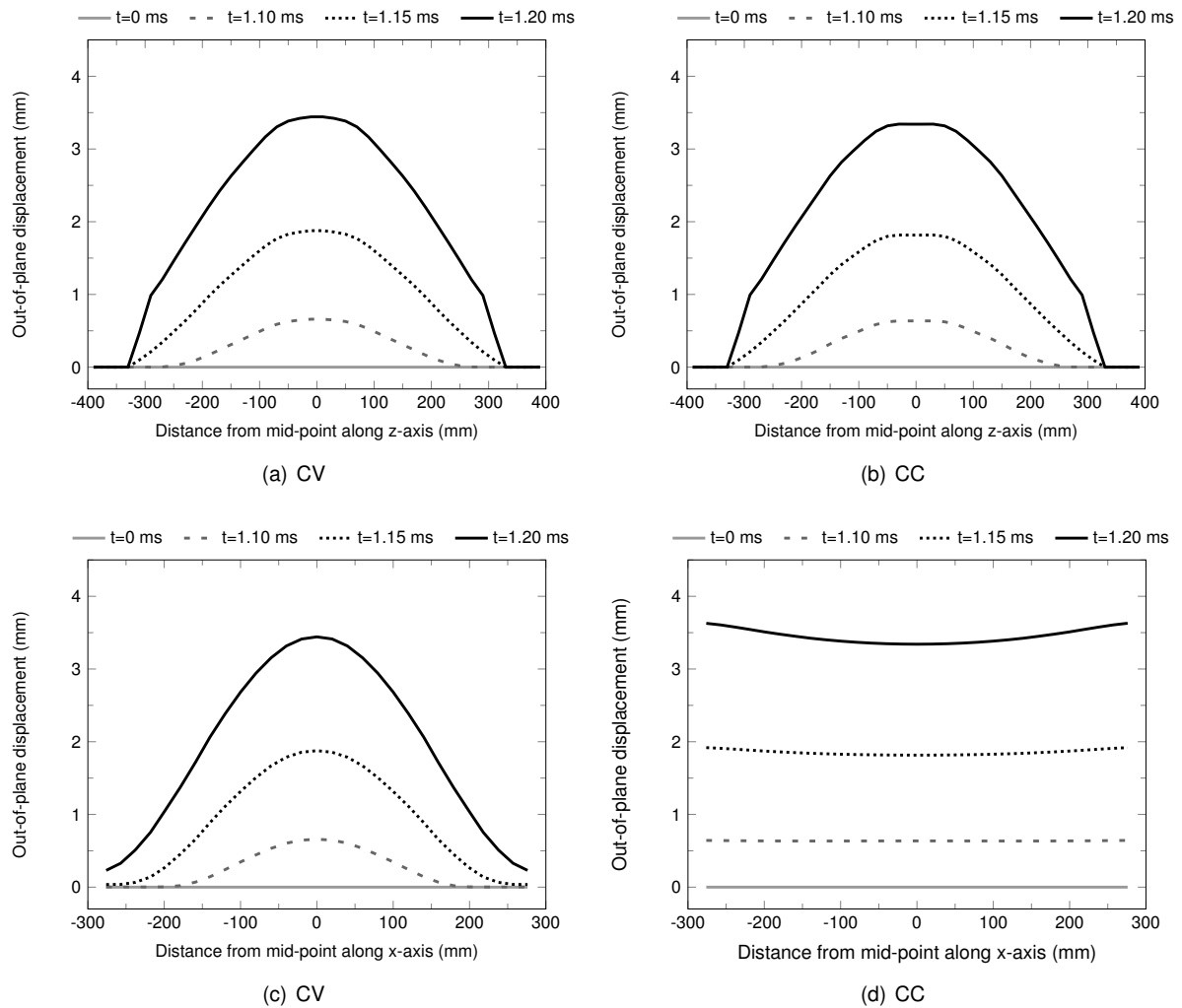


Figure 4.3: Time-history of the out-of-plane displacement along the z-axis for the (a) convex (CV) and (b) concave (CC) configuration and along the x-axis for the (c) CV and (d) CC configuration.

At each point of the system, the displacement comprises a part which relates to the rigid body motion of the panel, comprising the translation and rotation, and a part due to the strain. As the structures deform, there is a rapid degradation of the strength and reduction of the resistance to deformation of the panels due to the initiation of damage. The regions of response within the panel surface during the blast event result in different damage patterns depending on the geometric configuration. Therefore, an analysis of the failure extent and distribution for each particular failure mode will follow.

As previously mentioned, the ply failure of the laminate is modelled based on Hashin's failure criteria. Four different damage modes are considered, which comprise the failure of the fibres and matrix with separate mechanisms for tension and compression. In Abaqus [27], the initiation of damage is given by the output variables HSNFTCRT, HSNFCRT, HSNMTCRT and HSNMCCRT. The damage initiation criteria has been satisfied whenever any of the variables reach unity. For each mode, the damage is quantified by the output variables DAMAGEFT, DAMAGEFC, DAMAGENMT, DAMAGEMC, with an additional variable related to the damage due to shear, given by DAMAGESHR. An element is fully damaged whenever the damage variable for each of the failure modes reaches 1.0. Abaqus allows

the user to specify a maximum degradation value by selecting the element deletion option. When the damage variable for each element reaches the maximum degradation value (set to 1.0 in this work), damage evolution will stop and the element will be deleted from the mesh.

The contour plots for the four damage variables for each ply of the laminate at the end of the blast loading are shown in Figures 4.4 and 4.5 for the concave and convex cases, respectively. The position of the layers relative to the midplane were found not to have a great impact on the level of damage in the laminae and therefore, only the contour plots of the first four plies (from inner/incident to outer surface) are presented. In the figures,  $\theta$  denotes the relative orientation of the fibres with respect to the Z-axis.

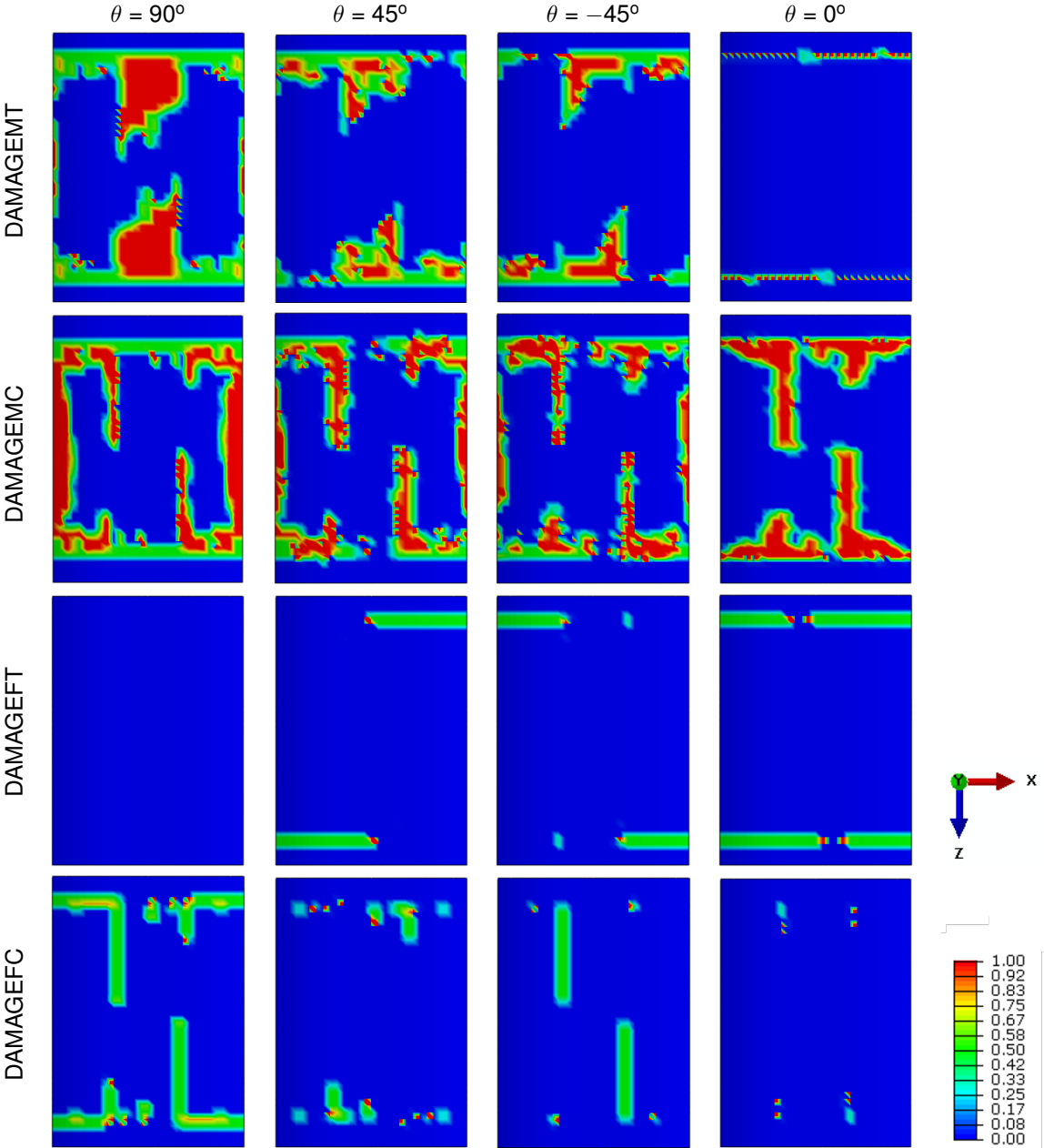


Figure 4.4: Surface distribution of damage in each ply for the concave configuration by the end of the blast loading ( $t = 2.0$  ms).

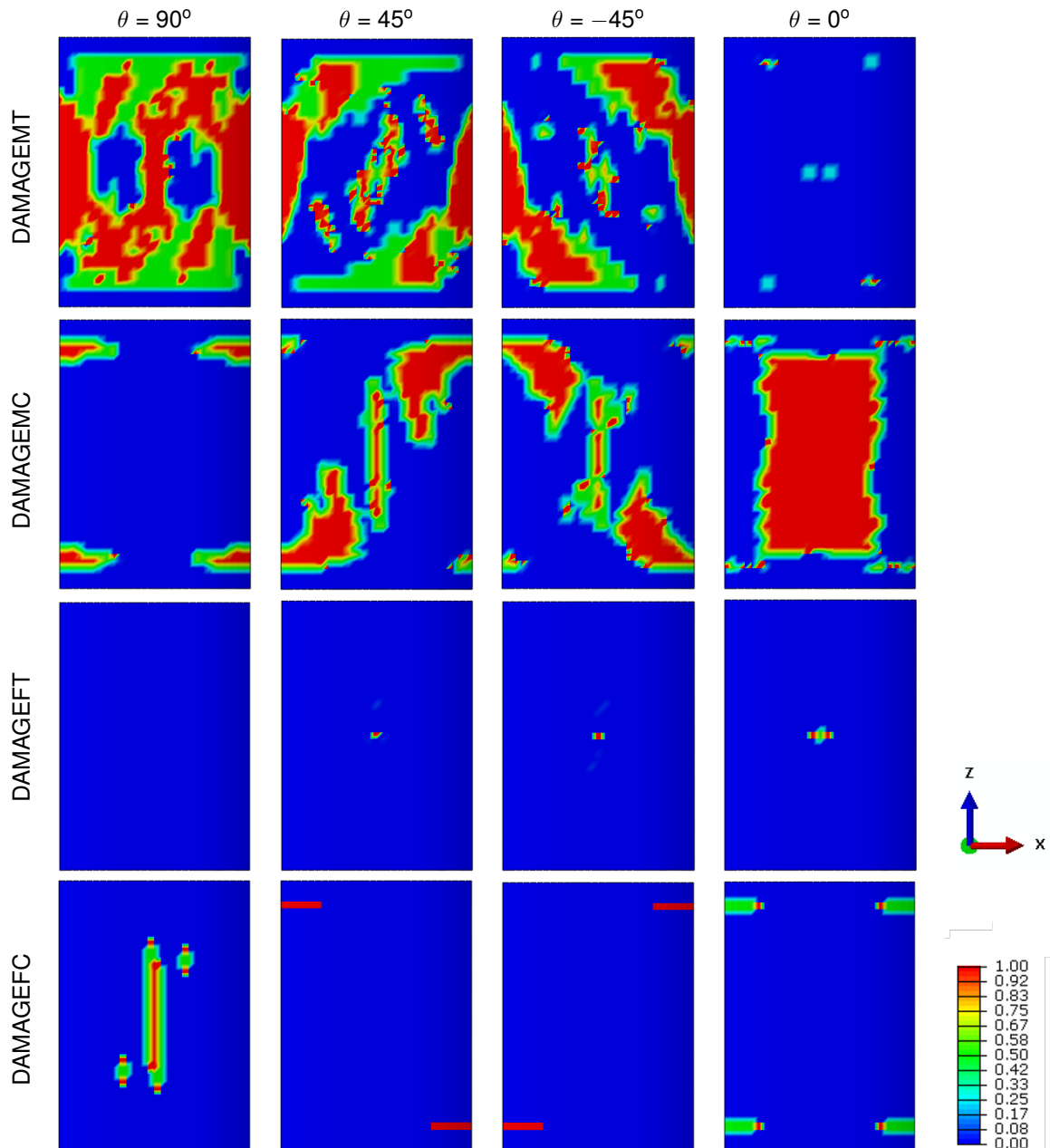


Figure 4.5: Surface distribution of damage in each ply for the convex configuration by the end of the blast loading ( $t = 2.0$  ms).

As expected, ply orientation and the geometry of the contact surface have an influence on the initiation and evolution of damage in the laminate. For the concave surface, damage in the matrix in the form of cracking and crushing, due to the matrix tensile and compressive modes, respectively, appear at  $t=1.21$  ms and  $t=1.24$  ms in the plies with the fibres oriented at  $90^\circ$  along the fixed edges of the surface. Damage initiation in the fibres occurs later in the deformation process, but in the same region where matrix damage is observed. Fibre rupture under tension first occurs in the plies with fibres oriented at  $0^\circ$ , at approximately  $t=1.35$  ms, whilst fibre kinking, or microbuckling, under compression, initiates in the elements of the plies with fibres oriented at  $90^\circ$ , at  $t=1.41$ ms.

For the convex case, matrix crushing and cracking initiate in the elements of the plies with fibres oriented at  $90^\circ$ , at  $t=1.22\text{ms}$  and  $t=1.30\text{ms}$ , respectively, along the fixed region of the surface. Fibre kinking and rupture first occur in the plies with fibres oriented at  $0^\circ$  at  $t=1.36\text{ms}$  and  $t=1.98\text{ms}$ , respectively. For the latter mode, however, fully-damaged elements are restricted to the central region of the surface.

From Figures 4.4 and 4.5 it is evident that despite geometric configuration, the extent of damage associated with matrix failure is higher than what is observed for fibre failure. This is due to the fact that the strength parameters associated with matrix failure are lower when compared to the fibre strengths, resulting in an overall improvement of the resistance to damage due to the fibres.

As it is known, in composite materials, the fibres are responsible for carrying the loads, enhancing the performance of composite structures regarding the strength properties. Therefore, damage in the fibres compromises the structural integrity of the panels and is followed by a rapid decrease of the strength, resulting in the complete rupture of the structures. This is observed for the concave configuration where, shortly after the blast loading, the complete failure of the structure is observed due to the damage along the fixed edges of the panel.

Moreover, the results observed regarding the initiation and evolution of damage for each configuration support the observations made with respect to the loading characteristics and resulting deformation modes stated above. It is important to consider the damage caused by the influence of local deformation due to a concentrated load, as well as by the progressive damage caused by the degradation of strength due to the bending and membrane stresses in the global region of response of the panels.

For the convex configuration, damage in the matrix initiates on the fixed boundaries due to the contribution of membrane and bending stresses. However, as stresses are more evenly distributed across the surface, the damage rapidly progresses to the centre of the panel, where higher deformation is found due to the deflection pattern observed. Later in the blast event, fully damaged elements associated with the fibre failure modes are observed in the centre region, at a time point in which the panel is at its maximum deflection.

For the concave case, stress will concentrate on the fixed edges of the panel, resulting on the initiation of matrix and fibre damage in these areas. As the panel further deforms, damage will progress along the free edges (where higher values of out-of-plane displacement are found) and, to a lesser extent, to the centre of the panel. The axial reaction forces in the fixed boundaries of the panel alternate between compressive and tensile, which indicates that the relative contribution between bending and membrane stresses is not the same throughout the loading from the shock wave, as the panels go from a bending dominated to a coupled bending-stretching regime.

In order to have an additional insight on the dynamic response of the panels and to assess the accuracy of the numeric model, an energy analysis will follow. The energy balance using the total energy ( $E_{total}$ ) quantities computed by Abaqus [27] is given by

$$E_{total} = E_{KE} + E_{VD} + E_{IE} - E_{WK} \simeq constant, \quad (4.1)$$

where  $E_{KE}$  is the kinetic energy,  $E_{VD}$  is the viscous energy dissipated  $E_{WK}$  is the work done by the

externally applied loads and  $E_{IE}$  is the internal energy, defined by

$$E_{IE} = E_{SE} + E_{AE} + E_{DMD}, \quad (4.2)$$

where  $E_{SE}$  is the (recoverable) elastic strain energy,  $E_{AE}$  is the artificial strain energy and  $E_{DMD}$  is the energy dissipated by damage.

The time histories of the terms of the total energy presented in Equation (4.1) for both conditions are shown in Figure 4.6.

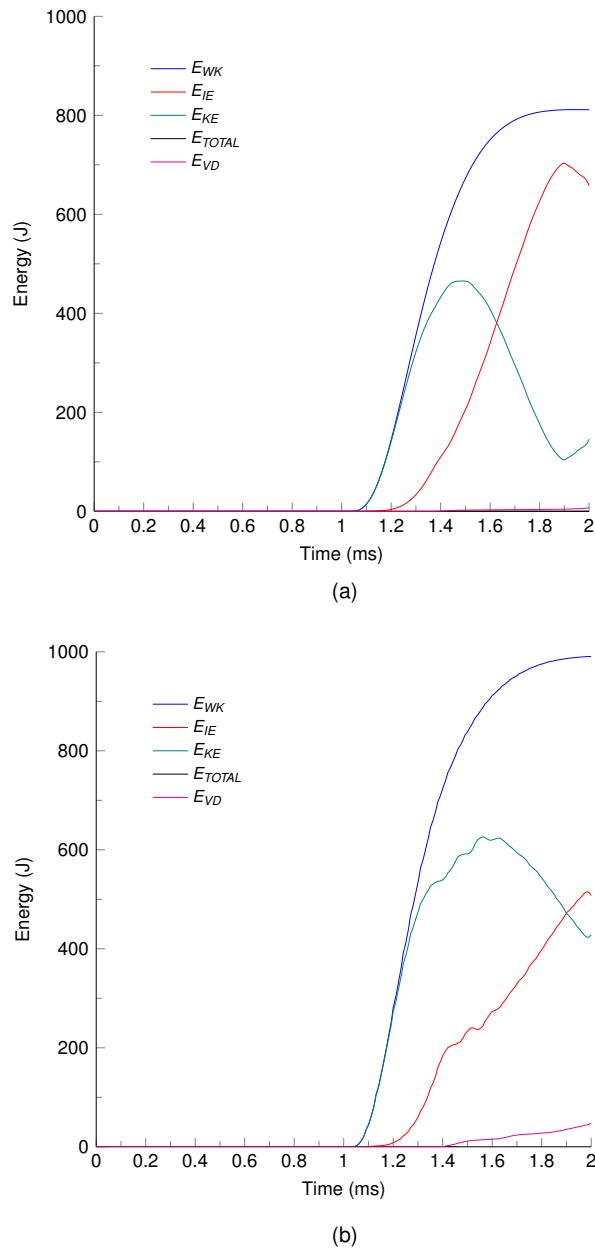


Figure 4.6: Total energy time history of the model for the (a) convex and (b) concave configuration.

In nonlinear problems,  $E_{total}$  should be only approximately constant. The approximation is due to the fact that the elastic strain energy,  $E_{SE}$ , is computed by a modified trapezoidal rule, rather than an exact



trapezoidal rule (which is not implemented due to computational performance implications) [27]. In the simulations, the total energy presents low variations, which are very small when compared to the other meaningful energies, and therefore the energy balance is clearly maintained throughout the analysis.

The energy dissipated by viscous effects,  $E_{VD}$ , is nonzero during the simulation, which indicates that there is some damping present. This is due to a standard bulk viscosity damping introduced to improve the modelling of high-speed events in Abaqus [27], with the default value for the quadratic bulk viscosity parameter and the linear bulk viscosity parameter being 1.2 and 0.06, respectively.

The kinetic energy,  $E_{KE}$ , increases and reaches a maximum value at an early stage of the blast event, and then, decreases. In contrast, the internal energy,  $E_{IE}$ , increases from zero and exhibits small oscillations before reaching a local maximum value. These oscillations are the result of element strength degradation in virtue of the initiation of damage in the laminate.

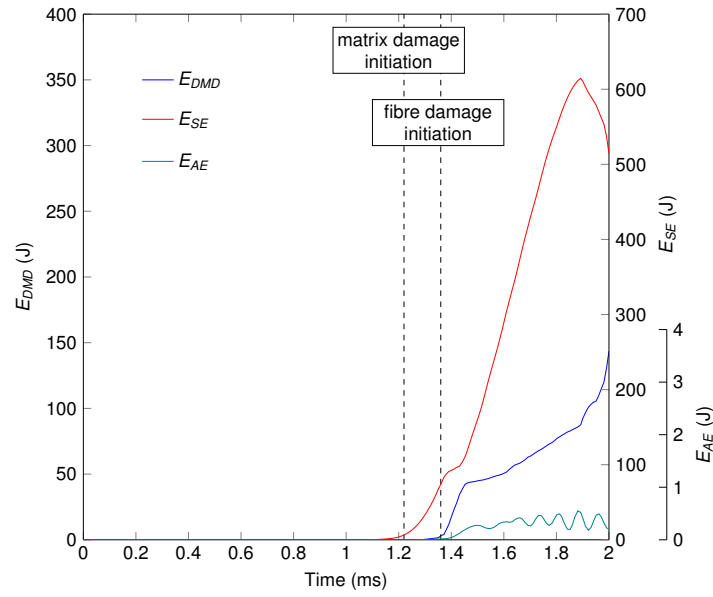
For the convex surface, more energy of the work done by the external forces is converted into internal energy, when compared to the concave model. This results in a rapid decrease in the kinetic energy. The components of  $E_{IE}$  are presented in Figure 4.7.

Initially, the internal energy of the panel only consists of the energy stored as elastic strain energy, that will increase as the panel elastically deforms. Following the initiation of damage in the panel, there is a component associated with the dissipation of energy due to the damage modes.

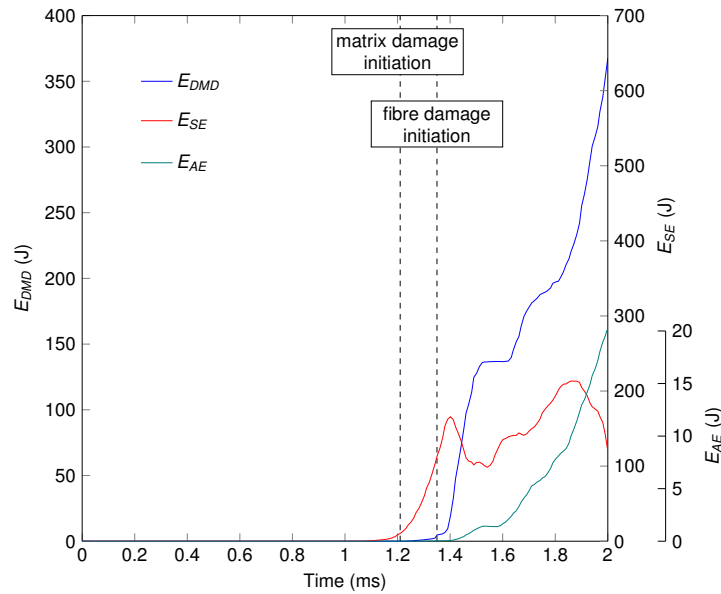
For each case, the damage associated with both modes of matrix failure is found not to have a major contribution to the energy dissipated by damage. In fact, when considering the variation of  $E_{DMD}$  in Figures 4.4 and 4.5, it is possible to observe that it shows a rapid increase shortly after the initiation of damage in the first mode associated with fibre failure. For the same time instants, the concave surface presents higher values of energy dissipated by damage when compared to the convex surface. This further supports the previous observations which showed that under the concave condition, the panel shows more fibre kinking and rupture associated to the fibre damage modes in compression and tension, respectively.

It is possible to observe that  $E_{SE}$  increases from zero until a local maximum, as the panels deform. For an undamaged structure, the deformation on the panel is built up until a point of maximum deflection is reached, in which the value of  $E_{SE}$  is maximum and the panel is almost entirely at rest, causing the kinetic energy to be at a minimum. After this instant, the structure tends to regain the initial configuration, as it oscillates. However, as the blast-induced damage increases, the loss of strength in the damaged elements reduces the ability of the panels to withstand further elastic deformations, leading to the complete failure of the structure.

In Figure 4.7, it is possible to observe that the maximum value of  $E_{SE}$  is reached at different time points for each configuration. For the convex surface, the local maximum value of elastic strain energy matches the local maximum of the internal energy,  $E_{IE}$  and the local minimum of the kinetic energy,  $E_{KE}$ , as seen in Figure 4.6 (a). Thus, it is possible to conclude that, for this configuration, the panel is mainly in the elastic regime, being at its point of maximum deflection, and the damage in the composite laminate still does not present a major influence in the deformation process.



(a)



(b)

Figure 4.7: Time history of the components of the internal energy for the (a) convex and (b) concave configuration.

For the concave configuration, however,  $E_{SE}$  presents a first local maximum earlier in the blast event, and the same relation is not observed. In this case, the extent of damage associated to the four failure modes of the composite laminate is more noticeable, as seen in the curve of  $E_{DMD}$  in Figure 4.7 (b). This results in a meaningful loss of strength of the panel which reduces the capability to decrease the kinetic energy during the blast event.

This further demonstrates the previous observations made regarding the effects of damage initiation and distribution for each surface. The blast mitigation capabilities of the convex configuration result in the delay of the initiation of damage on the fibres and the panel is able to extend the deformation in an (almost-) elastic regime, whereas in the concave specimen, the concentration of stress along the fixed

edges of the panel favours the initiation of fibre damage along these areas, enhancing the degradation of strength on the elements and ultimately leading to the complete failure of the structure.

Shortly after the shock wave impingement, for the concave configuration,  $E_{SE}$  sharply decreases and takes on negative values. Abaqus/Explicit tends to remain stable for most elements and circumstances. However, the sharp loss of material integrity in virtue of a rapid material softening due to the damage initiation and growth in the composite material results in large local nonlinearities and presents a challenge to obtain converged solutions for the simulations. When the amount of damage reaches a certain level, the numerical instabilities result in nonphysical solutions [27]. Therefore, it is considered that, at the time the value of  $E_{SE}$  shows a rapid decline (at around  $t = 2.0$  ms), the level of damage on the panel reaches a critical level and the structure no longer sustains any more loads and collapse occurs.

The artificial strain energy,  $E_{AE}$ , includes energy stored in hourglass resistances and transverse shear in shell elements. The ratio of the artificial strain energy,  $E_{AE}$ , to the internal energy,  $E_{IE}$ , is below 5% (as it should [27]) in the entire process of the structural response until failure, which is indicative of the accuracy of the numerical model. It should be referred that this relation was verified in all numerical models developed in the scope of this work. The ratio of  $E_{AE}$  to  $E_{IE}$  for the duration of the blast loading for the convex and concave cases is shown in Figure 4.8.

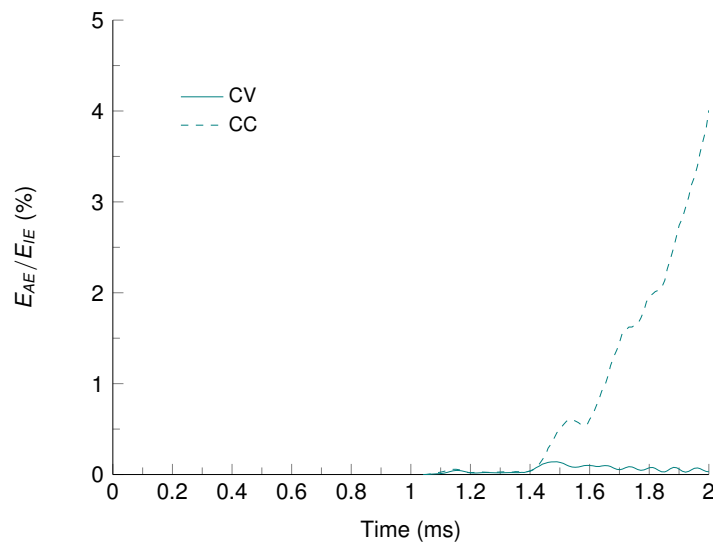


Figure 4.8: Time history of the ratio of artificial strain energy to internal energy for the convex (CV) and concave (CC) configuration.

It is important to notice that, despite the configuration, the CFRP panels are only able to dissipate energy due to the damage on the laminate and damping due to viscous effects. The inability to dissipate energy due to plastic deformation restricts the blast mitigation capability of the panels, introducing a conflict when using FRP composites at risk of explosive blast, as structures are expected to undergo deformations with no collapse, limiting the penetration of the panels and maximizing the dissipation of energy from the blast wave. The elastic brittle behaviour observed in this study makes clear the necessity to find alternatives so that both criteria can be met. As such, a study into the influence of geometric parameters, in this case, curvature and the addition of longitudinal stringers, will be presented next.

## 4.2 Influence of panel curvature on the blast response

For the purpose of analysing the effect of the curvature on the resistance of CFRP panels to blast loading, a group of panels with different radii of curvature, namely 500, 750 and 1000 mm, was investigated. All other dimensions ( $L$ ,  $t_s$  and  $a$ ) of the panels remained the same as those of the reference panel and therefore the section area ( $SA = 560 \text{ mm}^2$ ) and mass ( $m = 686 \text{ g}$ ) were identical for all configurations. For simplicity reasons, the panels with radii of curvature of 500, 750 and 1000 mm will be referred to as panels R500, R750 and R1000, respectively.

The panels were subjected to the shock waves resulting from the explosive blast of two distinct charges with an equivalent mass of TNT,  $W_e$ , of 60g and 100g, located at the same stand-off distance ( $SOD = 1 \text{ m}$ ). The shock waves were set to impact the concave surface of the panels, as this configuration was found to have the worst resistance to the blast.

For the purpose of discussion, the maximum value of the work of the external forces,  $E_{WK}$ , for each radii of curvature under the different blast conditions is displayed in Figure 4.9.

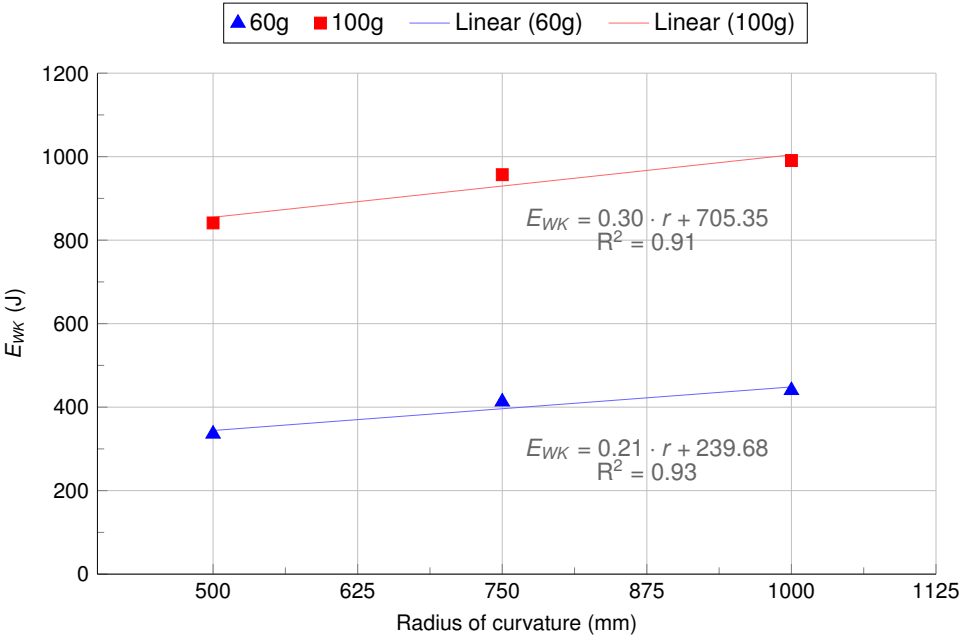


Figure 4.9: Maximum value of  $E_{WK}$  per radius of curvature,  $r$ , for charge masses of 60g and 100g of TNT.

For the range of blast conditions considered, the work of the external forces is the highest for the panel with the biggest radius of curvature (R1000) and lowest for the panel with smallest radius (R500), which is a direct result of (i) lower transferred loads to the structure in virtue of the increase of curvature and (ii) different deformation histories for each model. Similar results have been reported in the works of Qi et al. [8] and Kumar et al. [16].

Additionally, it can be seen that the influence of the curvature on the blast response of the curved panels appears to decrease with the reduction in charge masses. The trend lines for each mass of explosive charge show that the slope of the linear regression for  $W_e = 100 \text{ g}$  is higher than for  $W_e = 60 \text{ g}$

(by about 43%), which indicates that the blast mitigation properties in virtue of the increased curvature of the panels will be more significant with increasing blast loads.

As expected, the curvature of the panels has an influence on the load acting onto the surface. This is due to the fact that the curvature changes the reflective angle of the shock wave. As described in Section 2.1.5, the CONWEP algorithm uses the reflective angle to calculate the pressure that is applied onto the surface of the panel according to Equation (2.8). Bigger radii of curvature (i.e., flatter surfaces) result in a smaller reflective angle and therefore, higher values of effective pressure (and therefore impulse), are transferred to the panel.

In the early stage of the blast event, the average displacement on the surface of the panels is very similar. However, as the panels further deform, the difference between the out-of-plane displacements for each configuration becomes noticeable. The deformation history of the models result of the contribution of (i) the geometric stiffness and (ii) the extent and distribution of damage associated to the laminate failure modes.

By increasing the curvature of the panels, the stiffness, which is a function of the second moment of area, will also increase, as a larger area of the section is located away from the panel neutral axis (see Figure 4.10), ultimately improving the resistance to deflection of the structures under blast loading.

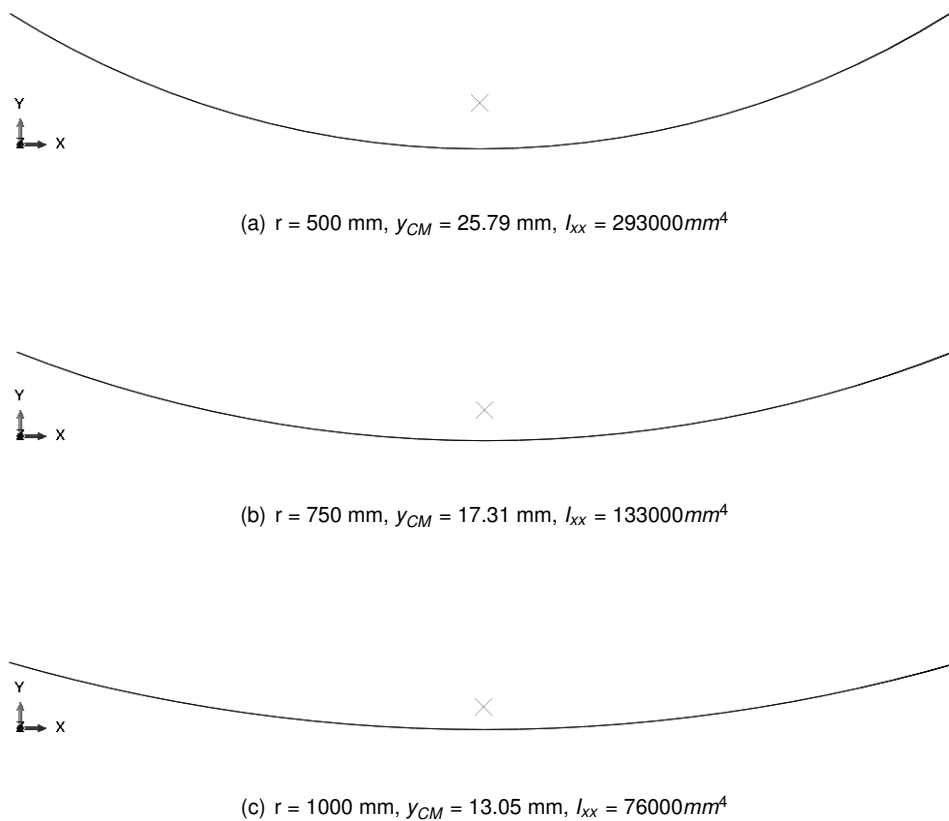


Figure 4.10: Influence of the curvature on the centre of mass height ( $y_{CM}$ ) and the second moment of area ( $I_{xx}$ ).

During the response of the panels to the dynamic blast loading, the curvature is seen to originate different deformation patterns. Whilst along the longitudinal direction the deformed shape is similar, along the circumferential direction, the panels exhibit different deformation shapes, as seen in Figure 4.11. For the R500 panel, the highest deformation is found to be located at the free edges of the panel, with the centre of the surface showing a lower value of out-of-plane displacement. Increasing the radius of curvature results in lower values of the out-of-plane displacement in the free edges and similar values in the centre of the panel, by comparison with the panels with bigger curvatures. This is due to the fact that, as the panel's curvature increases, the shock wave first impacts the free edges of the surface and continues to progress towards the centre along the normal direction.

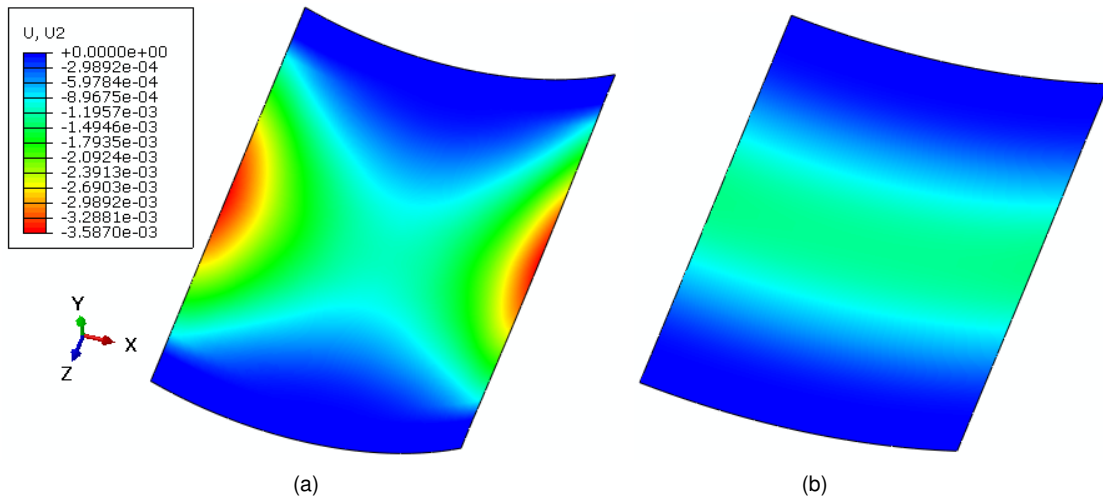


Figure 4.11: Deformed shapes of panel (a) R500 and (b) R1000 prior to damage initiation ( $t = 1.13$  ms).

As noted previously, the deformation response of the panels is influenced by the additional geometric stiffness provided by increasing curvatures. As such, it is expected that this translates into lower local maximum values of elastic strain energy for the R500 panel and higher for the R1000 panel. Every configuration presents a similar first local maximum value of  $E_{SE}$  at a very early stage in the blast event (at a time instant after which the panels continue to deform), which is indicative of a significant contribution of damage to the dynamic response of the panels. Although the local maximum values of  $E_{SE}$  decrease for the lowest charge mass, following the lower average displacement found under this condition, a similar pattern is observed. Therefore, a further assessment into the extent and distribution of damage associated to the laminate failure modes is needed.

Moreover, as more energy is transferred to the structure, the R1000 panel presents more energy associated to the translation motion of the laminate, namely in the form of kinetic energy, what originates an oscillatory motion with higher velocities. This has a special importance in applications where the oscillatory motion of the panels must be limited in order not to harm the occupants of a given structure. The same results were observed despite the mass of explosive charge, with the R500 panel showing the lowest values of  $E_{KE}$  during the blast event and the R1000 panel the highest. Both statements are illustrated in Figure 4.12 (a) and (b).

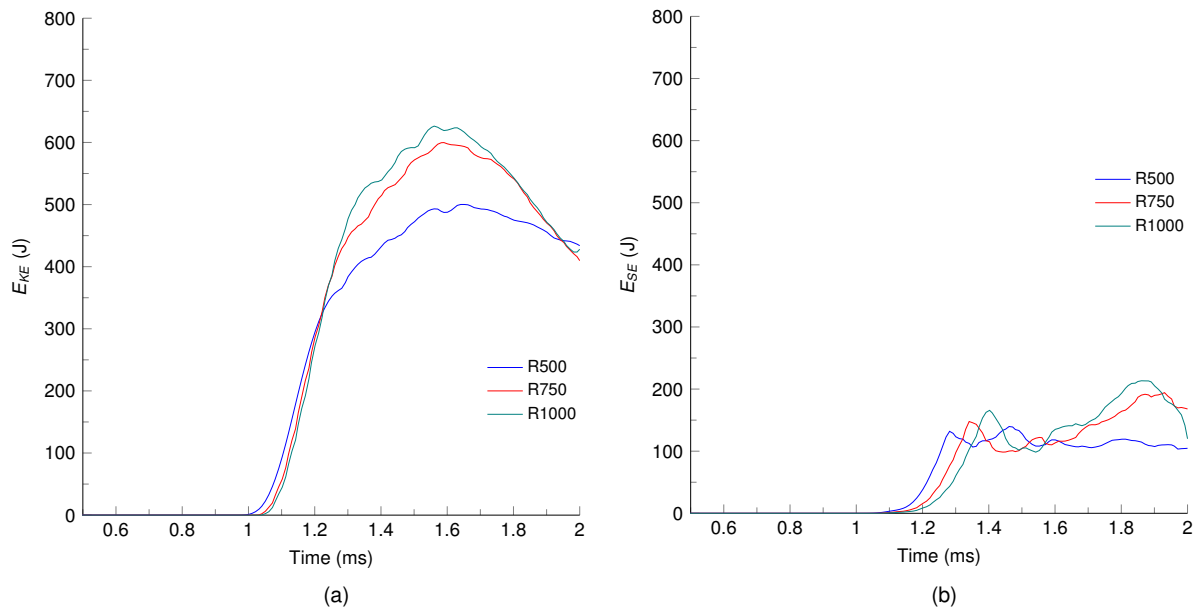


Figure 4.12: Time history of the (a) kinetic energy and (b) elastic strain energy for  $W_e = 100$  g.

As stated previously, the initiation of damage depends on the dynamic response of the panels, as stresses will concentrate in the areas where higher deformations are found. Moreover, the geometric stiffness induced by the curvature favours higher stresses on the surface of the panels as further bending is limited by the increased stiffness of the structures, leading to an earlier initiation of damage along the fixed edges. Therefore, the influence of curvature on the initiation and distribution of the failure modes will be assessed with more detail next.

For both blast conditions, damaged elements are first found in the R500 panel and last in the R1000 panel. All four failure modes were identified and followed the same progression sequence: damage due to matrix tension, matrix compression, fibre tension and fibre compression. It is thus possible to observe that the curvature influences the initiation of a particular failure mode whilst maintaining the same sequence. In order to quantify the damage induced by the explosion for each curvature, the percentage of elements fully damaged by the end of the blast loading for an explosive charge mass of 100 g is plotted in Figure 4.13.

As previously observed, the number of elements with damage associated to the two matrix failure modes, namely matrix cracking under tension and matrix crushing under compression, is higher than those fully-damaged due to the fibre failure modes. Moreover, more damage will be found regarding the failure of matrix and fibres in compression by virtue of the lower values of the compressive strength of the material in the longitudinal and transverse directions.

Regarding the curvature, the extent of the damaged areas in the panels under the same blast loading condition ( $W_e = 100$  g) is very similar irrespective of radii of curvature. For the lower explosive charge, analogous results were found, with the panels showing less fully damaged elements with regards to both the matrix and fibre damage modes.

Although damage initiates earlier for higher curvatures, a reduction in the curvature of the panels subjects them to higher loads and more energy acting on the surface. More impulse acting on the R1000 specimen leads to more energy available for the dynamic response of the panel and a rapid degradation of the stiffness of the structure due to the strains induced during the global deformation process. This is evident when taking into account the distribution of damage for each case, as seen in Figure 4.14. Note that, for simplification purposes, the results are shown as an envelope contour plot in which the maximum absolute values across all of the plies in the layup are considered.

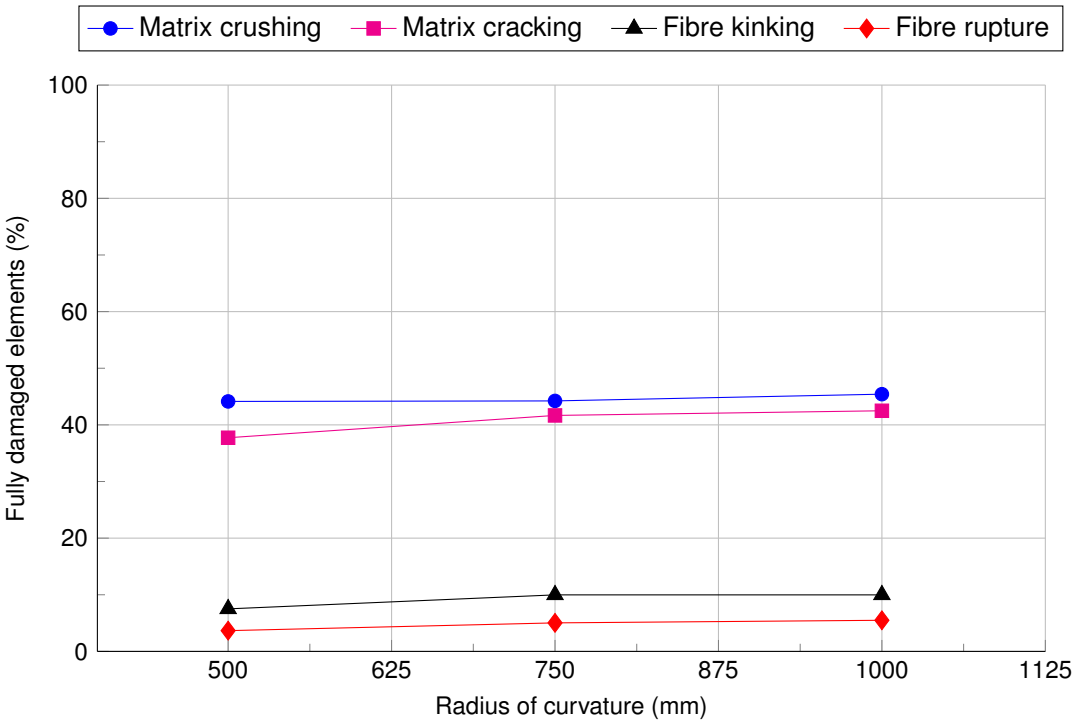


Figure 4.13: Influence of curvature on the percentage of damaged elements at the end of the blast loading for  $W_e = 100$  g.

In all panels it is observed that the damage progressed from the boundary of the laminates to the centre, with the damage associated with the two matrix failure modes being dominant. As the curvature increases, a predisposition towards more damage on the free edges becomes more evident. By decreasing the curvature, however, the damage spreads towards the centre of the panel, complementing the higher displacements found in this area.

For a charge mass of 100 g, shortly after the end of the blast loading (at approximately  $t=2$ ms), all the panels were considered to fail at sensibly the same time. A similar amount of damage in the elements originated a sudden decrease on the ability to elastically deform, resulting in a drop in the elastic strain energy, and the panels are considered to fail, as was previously mentioned. For the lower charge of 60 g, however, the damage that the panels withstand is not enough to compromise their structural integrity.



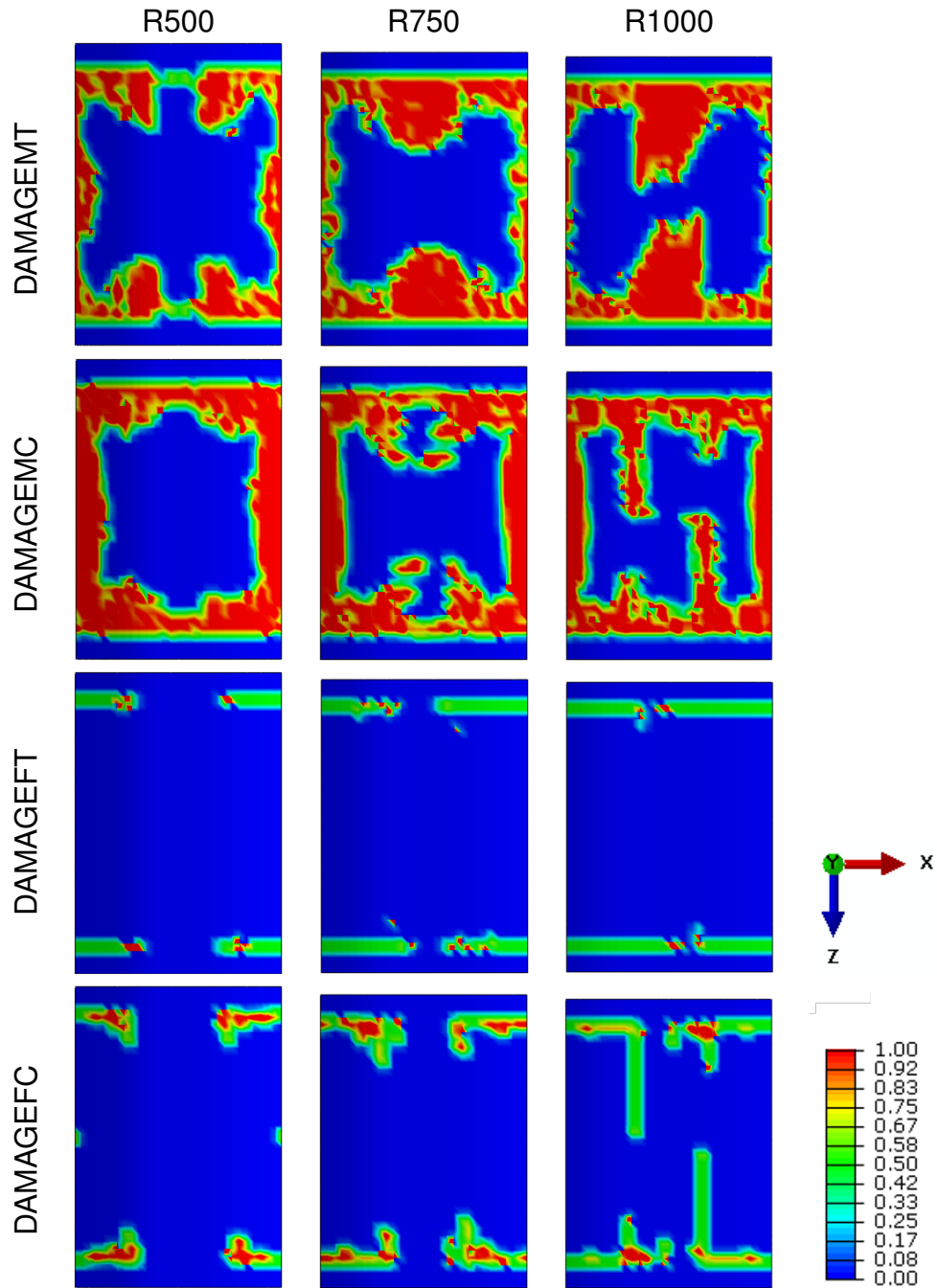


Figure 4.14: Influence of curvature on the surface distribution of damage for  $W_e=100g$  by the end of the blast loading ( $t = 2.0$  ms).

Finally, by analysing the behaviour of the panels aforementioned, it is possible to ensure that, for certain blast conditions below a loading threshold, the panel with higher curvature outperforms the remaining geometries, as it shows a higher capability to mitigate the loading under an explosive blast event, while showing an increased geometric stiffness. This evidence further supports previous studies [8, 16], in which curved panels were found to have the potential to exceed the performance of their flat counterparts under certain loading conditions.

### 4.3 Influence of structural reinforcements

This section aims to study the influence of stringer cross-section geometry on the blast performance of the reference CFRP panel with T-shaped stringers. Four other cross-sectional shapes were considered: I-, C-, J- and  $\Omega$ -shaped. The panels are identified by the shape of their stringers and henceforth, the panel with T-, I-, C-, J- and  $\Omega$ -shaped stringers will be referred to as panel T, I, C, J and  $\Omega$ , respectively. In each simulation, the concave surface of the panel is subjected to the same far-field blast conditions as in the previous sections ( $W_e = 100 \text{ g}$ ,  $\text{SOD} = 1 \text{ m}$ ).

The deformation process of the panels with stringers with the different cross-sections at the same time instant (prior to damage initiation) is shown in Figure 4.15.

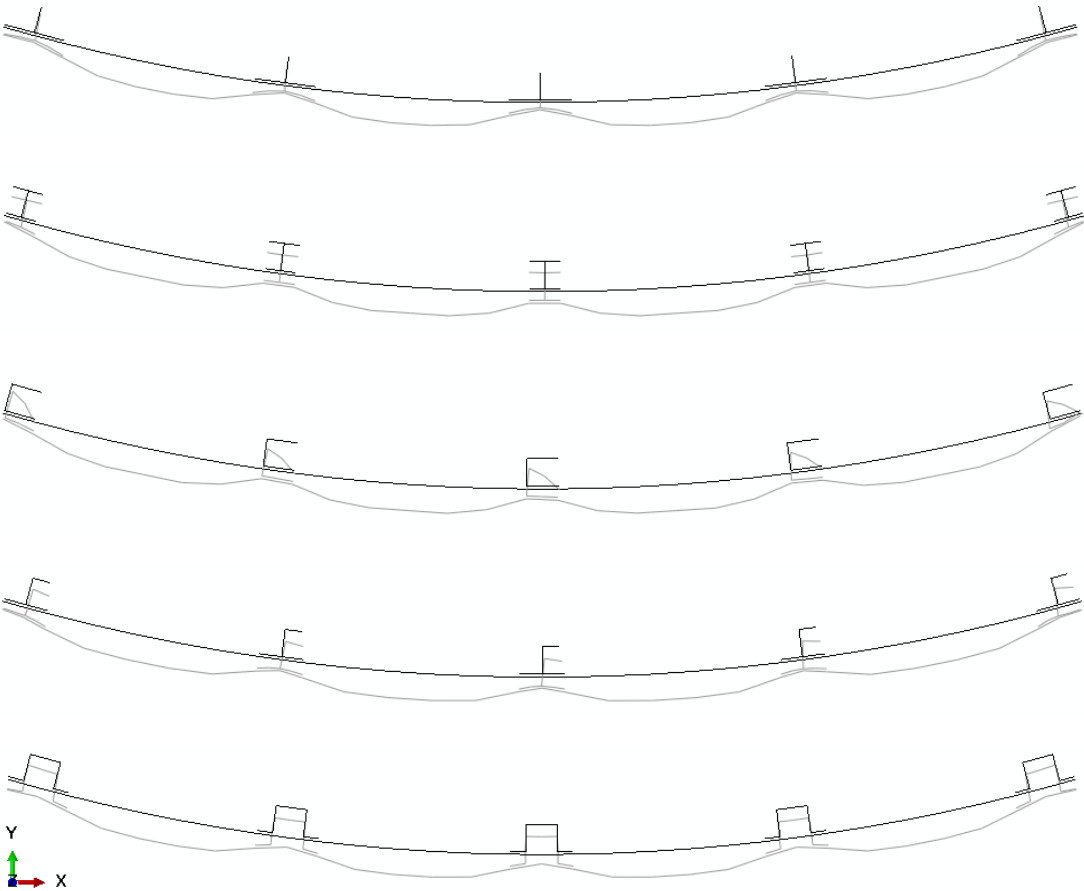


Figure 4.15: Deformed shapes of the five panels at  $t = 1.10 \text{ ms}$  (scale factors = 20, 20, 1, for X, Y, Z axes, respectively).

As expected, the introduction of longitudinal stringers in the panels resulted in an increased flexural stiffness which gave rise to lower values of deformation throughout the blast event. For all panels, the initial stiffness prior to damage initiation is the same, as every panel presents the same cross-sectional area. Additionally, the geometry of the stringers influences the projected area of the panel which will be under the influence of the blast loading from the shock wave, affecting the dynamic response of the panel, as will be discussed ahead.

As seen in Figure 4.15, the deformation pattern of panels T, I, C, J and  $\Omega$  is qualitatively identical. In the areas where the stringers are bonded to the skin, the deformed shape presents a local minimum of out-of-plane displacement whereas the maximum values are found in the "free" areas of the skin. At the same post-detonation time point prior to damage initiation,  $\Omega$  panel displays the lowest values of out-of-plane displacement in the skin and panel C the highest. Regarding the deformation of the stringers, it can be seen that the asymmetric stringers (with C- and J- shaped cross-sections) show coupled bending and torsion due to the fact that the shear centre of the stringers is not aligned with their centroid.

The panels show a reduction in the work of the external forces of 41.7-50.2% (depending on stringer configuration) in comparison to the panel with no stringers. The energy from the blast load will be transferred to both skin and stringers, which leads to lower global displacements as mentioned before. To further investigate the energy associated with the models, the time history of the kinetic energy and elastic strain energy for each stringer configuration is plotted in Figure 4.16 and compared to the values previously obtained for the panel without reinforcements.

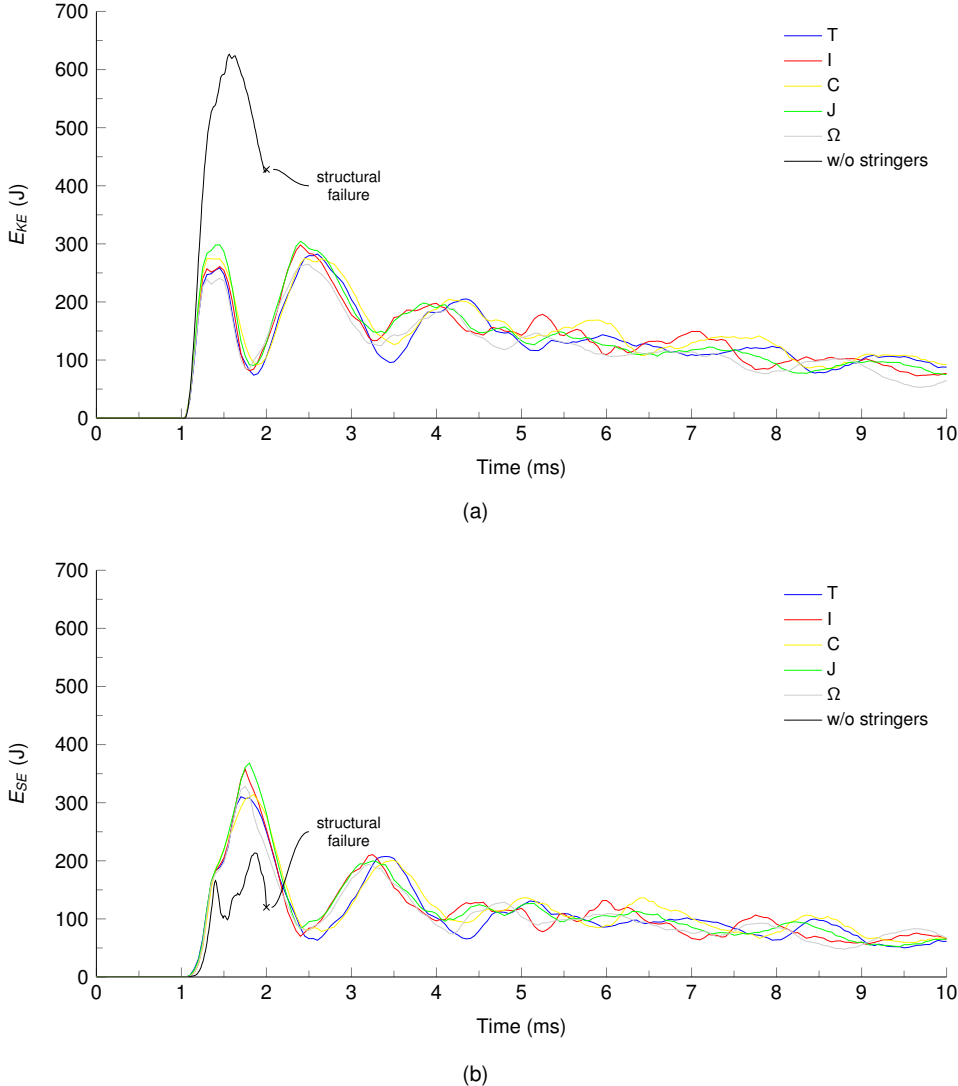


Figure 4.16: Time history of the (a) kinetic energy and (b) elastic strain energy for each model.

Regarding the kinetic energy, it is possible to observe that the addition of stringers into the panels results in a significant reduction of the global kinetic energy associated with the motion of the panels. The reinforced panels have a mass of approximately 1.8 times the mass of the panels without stringers. The reduction of the peak kinetic energy, however, does not follow the same proportion, with the ratio of the first local maximum value of  $E_{KE}$  for both cases ranging from 2.1 up to 2.6, depending on the geometry of the stringer's cross-section. This observation may be explained by the introduction of non-linearities in the simulations in virtue of the influence of the damage on the constitutive equations that govern the response of the panels. Moreover, it is possible that the influence of the shape of the stringers on the distribution of loads in the surface of the panels has an effect on the vibration modes of the models. It can be perceived that the additional stiffness provided by the reinforcements will result in an oscillatory motion with higher frequency and lower amplitudes.

By analysing the first local maximum value in the plots of Figure 4.16 (a), panel  $\Omega$  shows the lowest value of kinetic energy, with the panel J showing the highest. These observations are in agreement with the trend identified earlier regarding the maximum out-of-plane displacements for each cross-section shape. After this point, this relation is not maintained, as the influence of the damage on the laminate as well as the debonding of the adhesive layer will have an influence on the dynamic response of the panels.

In Figure 4.16 (b), the elastic strain energy gives an indication of the ability of the panels to elastically deform. As mentioned in the previous sections, the elastic strain energy is the work done to stretch the material. As the panels display more damage, the material loses its ability to store potential energy by virtue of the loss of strength associated to the failure modes on the composite laminate. It is possible to observe that the reinforced panels display higher values of  $E_{SE}$  during the blast loading event (up to, approximately,  $t = 2.0$  ms), when compared with the panels without reinforcements. After that point, the elastic strain energy (as well as the kinetic energy) will show oscillations due to the motion of the structure with decreasing amplitudes, as the panel slowly comes to rest.

To further investigate the observations made, a more in-depth analysis on the damage associated with the panels will follow. As discussed previously, an optimal configuration should be the one that minimizes the deformation of the panels while simultaneously minimizing the damage. Additionally to the laminate damage model governed by Hashin's criteria, the damage on the interface connecting the skin and stringers of the panel in the form of debonding was modelled using the nominal stress damage initiation criterion (MAXS). The damage initiation and evolution on the adhesive layer was obtained by the output variables CSMAXSCRT and CSDMG, respectively. When CSDMG reaches 1.0 in a point of the contact surfaces, there is a complete degradation in the adhesive and separation occurs.

The rapid initiation and progression of damage in the panels during the blast loading from the shock wave leads to an increase of the energy dissipated by damage. After the duration of the positive pressure phase of the shock wave, the energy dissipated by damage reaches a plateau and remains approximately constant. Figure 4.17 shows the total energy dissipated by damage in the skin, stringers and by the failure of the adhesive layer for each configuration.

Regarding the total value of  $E_{DMD}$  on the panels, it is possible to observe that the reinforced panels show a reduction of the energy associated to damage of 27.7% (panel J) up to 50.9% (panel  $\Omega$ ), when compared to the maximum value of  $E_{DMD}$  of the panel without stringers at the instant of collapse. As can be seen in Figure 4.17, the shape of the stringer highly influences the distribution of damage on the structure. As the shock wave impacts on the projected area of panels, the stringers with larger area of impact (J-,  $\Omega$ - and T-shaped) will withstand more damage (mainly associated with matrix crushing and cracking), whereas the remaining (I- and C-shaped) show the least. The damage in the skin follows an analogous relation, where the damage associated with the skin will be lower for the first case and higher for the latter, with the exception of the J-shaped stringers. For this configuration, the shock wave impinges both the top and bottom flanges, which will result in (i) higher deformations on the stringer and (ii) more energy passed to the skin. As it may be observed in the deformed shapes shown in Figure 4.15, the J- and T-shaped stringers show more deformation on the lower flange in comparison to the remaining configurations, which contributes, to a lesser extent, to the deformation and damage initiation on the skin.

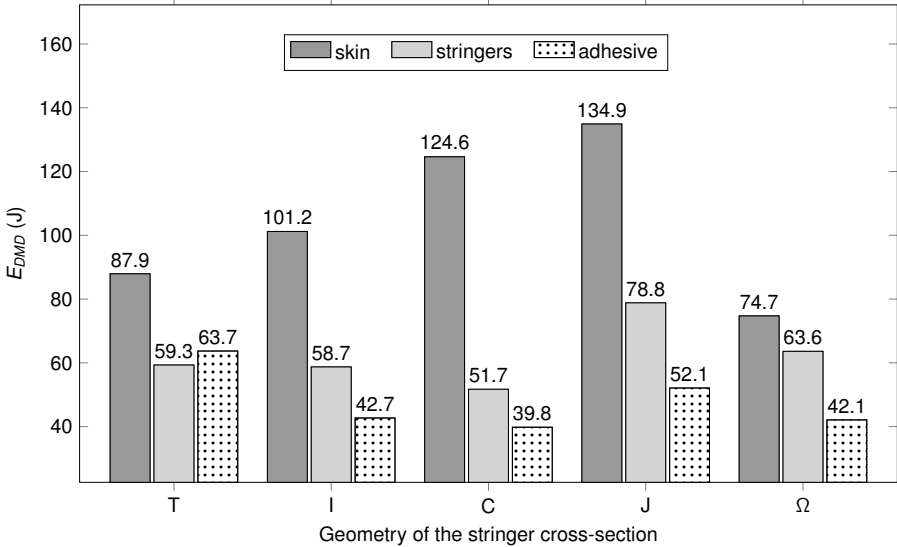


Figure 4.17: Energy dissipated by damage in the skin, stringers and adhesive interface for each configuration.

Debonding on the adhesive interface starts as soon as the shock wave arrives at the panel. For every panel, separation between the skin and stringers generally starts and progresses from the edges of the stringers into the centre, along the longitudinal direction. The stringers near the free edges of the panels are the first to show debonding in the entire contact surface, with the central stringer being the last. In Figure 4.18 the contour plot of the damage variable for cohesive surfaces (CSDMG) in the surface and in the deformed shape of the cross-section of the panel  $\Omega$  is shown.

The initiation and progression of damage in the adhesive will be strongly influenced by two main factors, being (i) the area of the surface of contact and (ii) the deformation modes of the stringers. This results in different levels of debonding for each configuration throughout the deformation process of the panels.

The stringers with T- and J-shaped cross-sections show more energy dissipated by the debonding in virtue of the larger area of the contact surface. In these cases, a larger area of contact will result in a stronger bonding in the skin-stringer interface. The remaining designs (I-, C- and  $\Omega$ -shape) show very similar values of energy dissipated, as these configurations present the same contact surface area. Additionally, the rotation of the C-shaped stringers were also found to benefit the debonding on the reinforcements.

Damage due to debonding starts at sensibly the same time on the adhesive layer and progresses at different rates, depending on stringer configuration. The  $\Omega$ -shaped stringers are the first to show cohesive damage on the entire contact surface, as this configuration shows the weakest adhesion to the surface of the panel. However, even for this case, the first stringer to be fully separated from the skin only appears near the end of the blast loading.

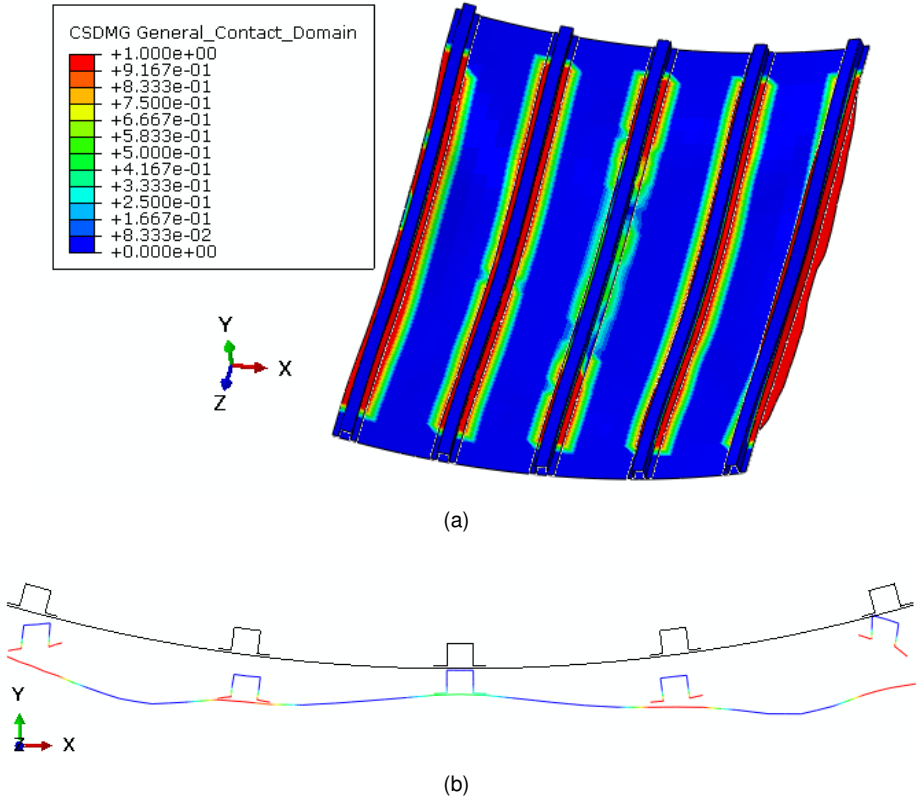


Figure 4.18: Debonding on (a) the surface and (b) the cross-section of the panel  $\Omega$  at  $t = 2.0$  ms.

The observations made so far further support the results regarding the kinetic energy of the panels after the first local maximum value (Figure 4.16 (a)), where the reduction in stiffness of the structure by virtue of the laminate damage and adhesive interface debonding are seen to have an influence on the oscillatory motion of the panels.

Following the analysis made regarding the blast resistance and response of the reinforced panels, it is shown that stiffeners present a viable solution to mitigate the effects of an explosive blast on curved CFRP panels. For the range of designs considered, panel  $\Omega$  shows the best results, once it shows (i) the lowest global maximum out-of-plane displacements and (ii) the least amount of structural damage.

These results are mainly due to the combination of a symmetric cross-section and bigger projected surface of the stringer (comprising both the top and bottom flanges). At the very beginning of the blast event, where the shock wave's overpressure value is maximum, this configuration successfully contributes to (i) less pressure loading acting directly on the skin of the panel and (ii) higher loads applied to the top flange, resulting in higher deformations and damage on the stringers instead of the panel's skin. Though this configuration shows a faster debonding on the adhesive interface, as the pressure from the shock wave exponentially decreases with time, the advantages of the stringer-skin bonding at latter stages of the blast event become less relevant and panel  $\Omega$  still outperforms the remaining configurations.





## Chapter 5

# Conclusions

This work aimed to contribute to a better understanding of the effects of the complex nature of blast actions on carbon fibre-reinforced polymer (CFRP) laminate single-curved panels used in aerospace applications.

A finite element model and analysis was accomplished using the commercial software Abaqus/Explicit (version 6.14). The CONWEP model implemented in Abaqus was used to simulate the shock wave originated by the explosive blast of a charge of TNT in free-air far-field conditions. This approach allows to realistically simulate overpressure amplitudes (including positive and negative phases) and does not require a fluid medium to account for shock wave propagation, resulting in an accurate and computationally efficient alternative to model an explosive blast. However, it is unable to account for the phenomena associated to near-field and semi-confined blasts, which include the effects of reflective waves and fireballs during an explosion.

The numerical model considered the in-plane mechanical properties of the composite laminate given by the matrix and fibres, which control the deformation and damage sustained by the panels. The damage initiation and evolution in the panels was modelled using the Hashin failure criteria, which assumes four different damage modes, comprising the failure of the fibres and matrix with separate mechanisms for tension and compression. An approach to qualitatively capture the strain rate dependency in the composite material model allowed to assess the effects of high strain rates under explosive blast loading conditions on the mechanical properties of CFRP laminates. Additionally, the study of the influence of geometric parameters such as the curvature and reinforcement's shape on the blast loading of the panels provided an insight on passive protective design alternatives capable of mitigating the effects of the dynamic loads during a bombing event. The modelling of the debonding in the adhesive interface was accomplished through the implementation of a contact formulation based on the cohesive properties of the adhesive and on the maximum nominal stress criterion.

The numerical study was able to capture the deformation history, failure modes and energy variation of the models. The proposed model can thus be used to design or evaluate the performance of blast-resistant FRP composite structures under specific explosive blast conditions. In this chapter, the main conclusions of the numerical study are presented, followed by some suggestions for future work.

## 5.1 Concluding remarks

The geometry of the incident surface was found to have an influence on the blast resistance of the panels, as the loading distribution on the concave and convex surfaces resulted in an enhancement and diffusion, respectively, of the effects from the shock wave loading. Two distinctive stages of panel deformation were identified, namely an indentation regime governed by a local deformation due to a concentrated load, and a global regime, which comprises two modes of deformation, i.e., bending and stretching. The regions of response within the panel surface result in (i) different deformation histories and (ii) distinct damage patterns throughout the blast event.

Despite both (concave and convex) configurations presenting similar local maximum values of out-of-plane displacement, for the same blast conditions, the convex configuration was found to effectively delay the initiation of damage and reduce the degradation of strength due to damaged elements (mainly associated with the fibre damage modes) on the laminate. For the concave specimen, however, the blast loading and deformation regime of the panel favours the initiation and propagation of fibre damage along the fixed edges of the surface. As fibres resist the majority of the applied loads, failure in the form of kinking (compression) and rupture (tension) lead to a rapid degradation of the structural integrity and consequently collapse of the panel.

Blast resistant structures must be able to simultaneously limit the deformation and damage, while maximizing the dissipation of energy from the shock wave. Thus, the elastic brittle behaviour observed in the CFRP laminates presented a challenge for mitigating the effects of the dynamic blast loading. As such, a study into the influence of the curvature and stringer cross-section geometry was performed.

For the same blast conditions, three panels with different radii of curvature (500, 750 and 1000 mm) were analysed. For blast loadings which resulted in the collapse of the studied panels, the increase in curvature does not offer an additional benefit for blast mitigation purposes. For lower values of explosive charge below a loading threshold (in which the panels fail), however, the panel with higher curvature outperforms the remaining configuration as it is able to (i) reduce the effect of the shock wave loading as less energy is transferred to the structure and (ii) decrease the deformation during the blast event by virtue of an increased geometric stiffness.

Similarly to the curvature, the addition of longitudinal stringers to the panels increases the second moment of area, leading to a higher ultimate strength of the structure. By comparison with an unstiffened panel, the results prove the effectiveness of structural reinforcements in the blast resistant properties of the models by (i) lowering the overall deformation of the panel and (ii) reducing the blast-induced damage on the structure. Moreover, the geometry of the stringers (T-, I-, C-, J- and  $\Omega$ -shaped stringers were studied) was found to actively contribute to the distribution of loads throughout the surface of the panels, with the  $\Omega$ -shaped stringers outperforming the remaining designs.

## 5.2 Future developments

Further developments of the present work can be directed towards an experimental investigation of the blast response of the panels analysed, in order to assess the accuracy of the numerical models and possibly improve them.

Moreover, an investigation considering the pre-loading of the panels could be made in order to study the influence of cabin pressurization and compressive, tensile and bending loads acting on the panels, which realistically represent the conditions to which an aircraft fuselage is submitted during an in-flight bombing event.

In addition, the results found in this work regarding the design configurations capable of improving the blast resistance of the panels could be used to develop a sandwich shell capable of combining the advantages of the curvature and reinforcements of the composite laminate panels studied and the use of polymeric soft cores capable of improving the energy absorption capability of the structures.

Lastly, a fully coupled analysis could be implemented in order to overcome the limitations of the simplifications used in the current work, as the simulations do not include fluid-structure interactions such as reflective waves and dynamic pressure and neglect the thermal effects from an explosion. Thereby, a study of the blast response of the panels under a wider range of blast conditions could be achieved, which could include explosions in near-field conditions and the possibility to model an in-cabin explosion.



# References

- [1] Flight Safety Foundation. Aviation safety network. URL <https://aviation-safety.net/> (accessed in January 2021).
- [2] F. Masi. *Blast actions from high explosives. Studies on their simulation and effects*. MSc thesis in Mechanical Engineering, University of Florence, 2017.
- [3] J. N. Reddy. *Mechanics of Laminated Composite Plates and Shells*, pages 81–83. CRC Press, 2<sup>nd</sup> edition, 2004.
- [4] A. Baker, S. Dutton, and D. Kelly. *Composite Materials for Aircraft Structures*, pages 1–21. American Institute of Aeronautics and Astronautics, Inc., 2<sup>nd</sup> edition, 2004.
- [5] Airbus S.A.S. Safe operations with composite aircraft. *Safety first #18*, July 2014.
- [6] D. Backman and R. Gould. Blast response of a pressurized aircraft fuselage measured using high-speed image correlation. *Experimental Techniques*, 39, 12 2012.
- [7] R. Veldman, J. Ari-Gur, and C. Clum. Response of pre-pressurized reinforced plates under blast loading. *International Journal of Impact Engineering*, 35(4):240 – 250, 2008.
- [8] C. Qi, S. Yang, L.-J. Yang, S.-H. Han, and Z.-H. Lu. Dynamic response and optimal design of curved metallic sandwich panels under blast loading. *The Scientific World Journal*, 2014, 07 2014.
- [9] E. Wang, Q. Li, and G. Sun. Computational analysis and optimization of sandwich panels with homogeneous and graded foam cores for blast resistance. *Thin-Walled Structures*, 147, 02 2020.
- [10] S. Li, X. Li, Z. Wang, G. Wu, G. Lu, and L. Zhao. Finite element analysis of sandwich panels with stepwise graded aluminum honeycomb cores under blast loading. *Composites Part A: Applied Science and Manufacturing*, 80:1 – 12, 2016.
- [11] J. Shen, G. Lu, L. Zhao, and Z. Qu. Response of curved sandwich panels subjected to blast loading. *Journal of Performance of Constructed Facilities*, 25:382–393, 10 2011.
- [12] A. Mouritz. Advances in understanding the response of fibre-based polymer composites to shock waves and explosive blasts. *Composites Part A: Applied Science and Manufacturing*, 125:105502, 2019.

- [13] A. Gargano, K. Pingkarawat, M. Blacklock, V. Pickerd, and A. Mouritz. Comparative assessment of the explosive blast performance of carbon and glass fibre-polymer composites used in naval ship structures. *Composite Structures*, 171:306 – 316, 2017.
- [14] A. Gargano, R. Das, and A. Mouritz. Finite element modelling of the explosive blast response of carbon fibre-polymer laminates. *Composites Part B: Engineering*, 177:107412, 2019.
- [15] R. Batra and N. Hassan. Blast resistance of unidirectional fiber reinforced composites. *Composites Part B: Engineering*, 39(3):513 – 536, 2008.
- [16] P. Kumar, D. S. Stargel, and A. Shukla. Effect of plate curvature on blast response of carbon composite panels. *Composite Structures*, 99:19 – 30, 2013.
- [17] G. Sinclair. *The reponse of singly curved fibre reinforced sandwich and laminate composite panels subjected to localised blast loads*. MSc thesis in Mechanical Engineering, University of Cape Town, 2014.
- [18] R. Degenhardt, A. Kling, K. Rohwer, A. Orifici, and R. Thomson. Design and analysis of stiffened composite panels including post-buckling and collapse. *Computers Structures*, 86(9):919 – 929, 2008. Composites.
- [19] G. Pereira. *Computational modelling of failure of stiffened composite panels*. MSc thesis in Aerospace Engineering, Instituto Superior Técnico, University of Lisbon, 2017.
- [20] M. Silva. *Strength of aircraft composite panels under transverse impact loading*. MSc thesis in Aerospace Engineering, Instituto Superior Técnico, University of Lisbon, 2018.
- [21] H. Martins. *Comportamento mecânico de painéis compósitos de fuselagem sujeitos a ações de impacto: Influência do projétil, carregamento e taxa de deformação*. MSc thesis in Aerospace Engineering, Instituto Superior Técnico, University of Lisbon, 2021.
- [22] S. Giversen. Blast testing and modelling of composite structures. Technical Report S167, DTU Mechanical Engineering, 2014.
- [23] V. Karlos and G. Solomos. Calculation of blast loads for application to structural components. Technical report, Joint Research Center of the European Commission, 2013.
- [24] Design and analysis of hardened structures to conventional weapon effects. Technical Report UFC 3-340-01, U.S. Department of Defense, 2002.
- [25] D. Bongosian, M. Yokota, and S. Rigby. TNT equivalence of C-4 and PE4: a review of traditional sources and recent data. *24th Military Aspects of Blast and Shock Conference*, 2016.
- [26] C. N. Kingery and G. Bulmash. Air blast parameters from tnt spherical air burst and hemispherical burst. Technical Report ARBRL-TR-02555, U.S. Army Ballistic Research Laboratory, 1984.
- [27] Dassault Systèmes. Abaqus/CAE User's Guide (6.14). Providence, RI, USA, 2014.

- [28] M. Botez and L. Bredean. Numerical study of a RC slab subjected to blast: A coupled eulerian-lagrangian approach. *IOP Conference Series: Materials Science and Engineering*, 471:052036, 02 2019. doi: 10.1088/1757-899X/471/5/052036.
- [29] N. Naik and P. Shembekar. Elastic behavior of woven fabric composites: I—lamina analysis. *Journal of Composite Materials - J COMPOS MATER*, 26:2196–2225, 12 1992.
- [30] Q. Ahsan, Z. Mustafa, and S. Y. Chang. *Tribological Properties of Natural Fibre Reinforced Polymer Composites*, pages 347–381. Springer Singapore, Singapore, 2021.
- [31] Z. Hashin and A. Rotem. A fatigue failure criterion for fiber reinforced materials. *Journal of Composite Materials*, 7:448–464, 1973.
- [32] Z. Hashin. Failure criteria for unidirectional fibre composites. *ASME Journal of Applied Mechanics*, 47(2):329 – 334, 1980.
- [33] A. Matzenmiller, J. Lubliner, and R. Taylor. A constitutive model for anisotropic damage in fiber-composites. *Mechanics of materials*, 20(2):125 – 152, 1995.
- [34] A. Schlueter. *Phase Field Modeling of Dynamic Brittle Fracture*. PhD thesis, Department of Mechanical and Process Engineering, University of Kaiserslautern, 2019.
- [35] R. Zimmermann and R. Rolfes. Posicoss—improved postbuckling simulation for design of fibre composite stiffened fuselage structures. *Composite Structures*, 73(2):171 – 174, 2006. International Conference on Buckling and Postbuckling Behavior of Composite Laminated Shell Structures.
- [36] S. A. Tekalur, K. Shivakumar, and A. Shukla. Mechanical behavior and damage evolution in e-glass vinyl ester and carbon composites subjected to static and blast loads. *Composites Part B: Engineering*, 39(1):57–65, 2008. Marine Composites and Sandwich Structures.
- [37] A. Furqan, S. P. Santosa, A. S. Putra, D. Widagdo, L. Gunawan, and F. Arifurrahman. Blast impact analysis of stiffened and curved panel structures. *Procedia Engineering*, 173:487 – 494, 2017.
- [38] J. L. R. Comtois, M. R. Edwards, and M. C. Oakes. The effect of explosives on polymer matrix composite laminates. *Composites Part A: Applied Science and Manufacturing*, 30(3):181–190, 1999.
- [39] K. Tran, C. Douthe, K. Sab, J. Dallot, and L. Davaine. Buckling of stiffened curved panels under uniform axial compression. *Journal of Constructional Steel Research*, 103:140–147, 2014.
- [40] A. Winzen and R. Degenhardt. Simulation of stringer stiffened CFRP panels in consideration of skin-stringer separation. 04 2006.
- [41] P. Camanho, P. Maimí, and C. Dávila. Prediction of size effects in notched laminates using continuum damage mechanics. *Composites Science and Technology*, 67(13):2715 – 2727, 2007.
- [42] R. Krueger and P. Minguet. Analysis of composite panel-stiffener debonding using a shell/3D modeling technique. 01 2006.

- [43] K. Micallef, A. Soleiman Fallah, P. Curtis, D. Pope, and L. Louca. Constitutive formulation of strain-rate sensitive deformation in orthotropic composites. *WIT Transactions on Modelling and Simulation*, 51:397–408, 05 2011.
- [44] J. Schaefer, B. Werner, and I. Daniel. Strain rate effects on failure of a toughened matrix composite. *Conference Proceedings of the Society for Experimental Mechanics Series*, 6:117–123, 07 2014.